Published by Institute of Physics Publishing for SISSA
Received: *May 5, 2008*
Accepted: *May 28, 2008*
Published: *June 13, 2008*

The fast life of holographic mesons

Robert C. Myers[ab] **and Aninda Sinha**[a]

[a] *Perimeter Institute for Theoretical Physics, Waterloo, Ontario N2L 2Y5, Canada*
[b] *Department of Physics and Astronomy, University of Waterloo, Waterloo, Ontario, N2L 3G1, Canada*
E-mail: rmyers@perimeterinstitute.ca, asinha@perimeterinstitute.ca

Abstract: We use holographic techniques to study meson quasiparticles moving through a thermal plasma in $\mathcal{N} = 2$ super-Yang-Mills theory, with gauge group $\mathrm{SU}(N_c)$ and coupled to N_f flavours of fundamental matter. This holographic approach reliably describes the system at large N_c, large 't Hooft coupling and $N_f/N_c \ll 1$. The meson states are destabilized by introducing a small quark density n_q. Spectral functions are used to examine the dispersion relations of these quasiparticles. In a low-momentum regime, the quasiparticles approach a limiting velocity which can be significantly less than the speed of light. In this regime, the widths of the quasiparticles also rise dramatically as their momentum approaches a critical value $\mathfrak{q}_{\rm crit}$. While the spectral functions do not display isolated resonances for $\mathfrak{q} > \mathfrak{q}_{\rm crit}$, the dispersion relations can be extended into this high-momentum regime by studying the dual quasinormal modes. A preliminary qualitative analysis of these modes suggests that the group velocity rises to the speed of light for $\mathfrak{q} \gg \mathfrak{q}_{\rm crit}$.

Keywords: Gauge-gravity correspondence, AdS-CFT Correspondence.

JHEP06(2008)052

Contents

1. Introduction **1**

2. Holographic framework **4**
2.1 Black hole embeddings 6
2.2 Minkowski embeddings 6

3. Meson spectral functions **7**
3.1 Dispersion relations 10

4. Quasinormal modes **19**

5. Beyond $\mathfrak{q}_{\mathrm{crit}}$ **24**

6. Discussion **30**

A. WKB approximation **35**

1. Introduction

A large class of strongly coupled gauge theories can be studied using the gauge/gravity duality [1, 2]. The gauge theories that are currently amenable to study with holographic techniques are very different from real world QCD, e.g., current calculations are restricted to large N_c and large 't Hooft coupling. However, this approach has still proven to be a fruitful framework with which to gain new insights into the strongly coupled quark-gluon plasma — see, e.g., [3, 4].

With this aim in mind, holographic techniques have been applied to study the thermal properties of N_f flavours of fundamental matter in $\mathcal{N} = 2$ SU(N_c) super-Yang-Mills (SYM) in a quenched approximation (i.e., $N_f \ll N_c$) [5–8]. The gravity dual for this field theory consists of N_f probe D7-branes in the black hole background generated by N_c D3-branes. In this system, the fundamental matter generically undergoes a first order phase transition at some temperature T_{fun} . The low-temperature phase of the theory is described by 'Minkowski embeddings' of the probe branes (see figure 1) in which the branes sit entirely outside the black hole [6, 7]. In this phase, the meson spectrum is discrete and exhibits a mass gap. Above the critical temperature T_{fun}, the branes are characterised by 'black hole' embeddings which extend through the event horizon. In this phase, the meson spectrum is continuous and gapless [7, 9, 10]. Thus, this large-N_c, strong coupling phase transition is associated with the dissociation of the mesons. It has been suggested that this physics

JHEP06(2008)052

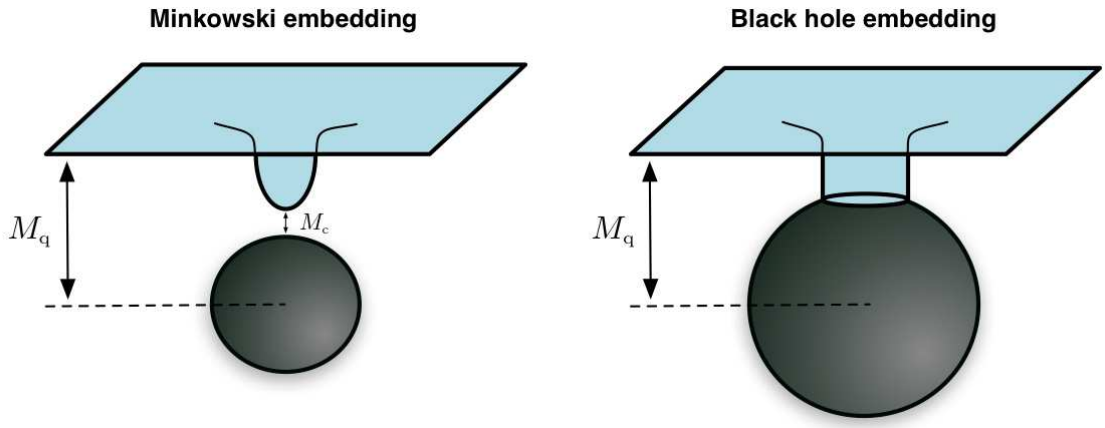

Figure 1: Possible embeddings for probe D7-branes in the background black hole geometry of D3-branes.

is in qualitative agreement with that of heavy quarkonium in QCD [7]. Studies from lattice QCD [11] suggest that such mesons survive the deconfinement phase transition at $T_{\rm dec} \sim 175\,{\rm MeV}$ and remain as relatively well-defined resonances up to temperatures of $2-3\,T_{\rm dec}$.

Another interesting feature that was discovered for the holographic mesons in the low temperature phase is that moving through the thermal plasma, at large momentum they approach a limiting velocity with $v_{\rm lim} < 1$ [7, 12]. On the gravity side, this can be understood as the dual excitations travelling at the local speed of light near the minimum radius reached by the D7-branes. Hence in the field theory, one finds the velocity

$$v_{\rm lim} = \frac{dx}{dt} = \sqrt{-g_{tt}/g_{xx}}\Big|_{\rho=\rho_{\rm min}} \tag{1.1}$$

Because of the redshift near the black hole horizon, this yields a result which can be much less than one. As discussed in [12], this result (1.1) can be re-expressed as

$$v_{\rm lim}^2 \simeq 1 - \frac{\lambda^2}{4}\left(\frac{T}{M_q}\right)^4 . \tag{1.2}$$

We must note that the limiting speed does not actually represent a 'speed limit' for the mesons. That is, a careful analysis show that the group velocity actually approaches $v_{\rm lim}$ from above and so the maximum group velocity is actually slightly larger than this asymptotic value [12]. In any event, the effect that $v_{\rm lim} < 1$ is somewhat surprising as one's naive intuition would be that a meson traveling through the thermal plasma would eventually reach the speed of light if the energy/momentum is increased to arbitrarily large values. Hence it appears that this new limiting velocity is a consequence of strong coupling.

As mentioned above in the low temperature phase, the holographic mesons are stable or rather their widths are suppressed by $1/N_c$. Of course, this stands in contrast with the

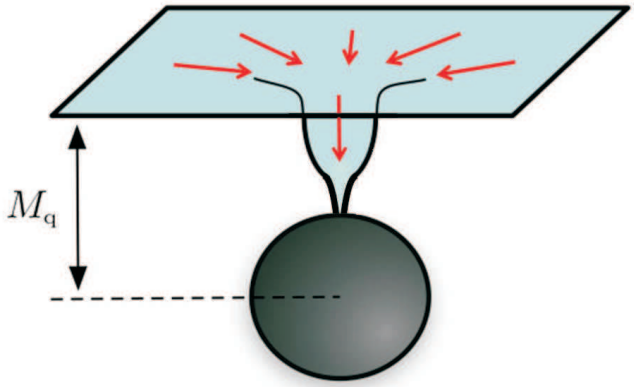

Figure 2: D-brane embedding with radial electric field is necessarily a black hole embedding but the width of the throat is tuneable.

heavy-quark mesons studied in thermal lattice QCD [11] which are quite broad states. In the black hole phase of the holographic model, the meson excitations are readily absorbed by the black hole horizon. The quasinormal frequencies of these excitations typically have $\mathrm{Im}(\omega) \sim \mathrm{Re}(\omega)$ [10] and so the corresponding spectral functions do not reveal any quasiparticles [9]. However, black hole embeddings can also arise at low temperatures when a nonzero quark density n_q is introduced[1] — in fact, these are the only physically consistent embeddings in this situation [13]. In these backgrounds, the meson states are again unstable but the width of these states can be tuned by varying n_q [14, 15]. Essentially, with a small n_q, the D7-brane extends down to the horizon with a narrow neck (as illustrated in figure 2) and so the absorption of the meson excitations is limited by the small effective horizon area of the worldvolume metric. Hence the corresponding spectral functions display clear quasiparticle states with narrow widths [15]. In this paper, we begin a study of the dispersion relations of these quasiparticle states.

An overview of the paper is as follows: in section 2 we introduce the D3/D7-brane framework and review the D7-brane embeddings and thermodynamics. In section 3, we turn to the calculation of the spectral function for various meson operators. By following the position and shape of the quasiparticle resonances in the spectral function with growing momentum, $\mathfrak{q}$, we estimate the dispersion relations for the low-lying resonances. With this approach, the quasiparticles are found to approach the same limiting velocity found for the case of stable mesons [7, 12].[2] Another interesting phenomena is that the widths show a dramatic increase as the momentum approaches a critical value $\mathfrak{q}_{\rm crit}$. section 4 presents a qualitative discussion of the quasinormal frequencies using our intuition derived from casting the relevant radial equation in the form of an effective Schrödinger equation. This framework gives an alternative point of view from which to understand the effects noted above. Above $\mathfrak{q}_{\rm crit}$, the spectral functions do not exhibit isolated quasiparticle resonances

[1]Since the the underlying theory here is supersymmetric, the quark density we consider arises from a hypermultiplet with both fermions and bosons.

[2]See also [16].

JHEP06(2008)052

and so in section 5, we use the Schrödinger framework to consider the behaviour of the quasinormal modes in the high-momentum regime $\mathfrak{q} > \mathfrak{q}_{\rm crit}$. In previous sections, we defined the limiting velocity $v_{\rm lim}$ by observing the (real part of the) dispersion relation approached a straight line for large $\mathfrak{q}$ but in the regime $\mathfrak{q} < \mathfrak{q}_{\rm crit}$. Here our qualitative analysis suggests that this definition fails in the regime $\mathfrak{q} \gg \mathfrak{q}_{\rm crit}$. Rather the behaviour of the dispersion relation changes such that ultimately it approaches an asymptotic slope of one in this very high momentum regime. In section 6, we discuss our results and make a few observations about future directions. Appendix A provides some details about a WKB calculation of the quasinormal frequencies using the Schrödinger framework considered in section 4.

2. Holographic framework

Following [6, 7], we write the background metric for $N_{\rm c}$ black D3-branes in the decoupling limit as

$$ds^2 = \frac{1}{2}\left(\frac{u_0\rho}{L}\right)^2\left[-\frac{f^2}{\tilde{f}}dt^2 + \tilde{f}d\vec{x}^{\,2}\right] + \frac{L^2}{\rho^2}\left[d\rho^2 + \rho^2 d\Omega_5^2\right]\,, \tag{2.1}$$

where ρ is a dimensionless coordinate and

$$f(\rho) = 1 - \frac{1}{\rho^4}\,, \quad \tilde{f}(\rho) = 1 + \frac{1}{\rho^4}\,, \quad L^4 = 4\pi g_{\rm s} N_{\rm c} \ell_{\rm s}^4\,. \tag{2.2}$$

This metric possesses a horizon at $\rho = 1$ with temperature

$$T = \frac{u_0}{\pi L^2}\,, \tag{2.3}$$

which is identified with the temperature of the dual $\mathcal{N} = 4$ SYM theory. Further the coordinates $\{t, \vec{x}\}$ are identified with the coordinates of the gauge theory. The string coupling constant is related to the SYM 't Hooft coupling constant through[3]

$$\lambda = g_{\rm YM}^2 N_{\rm c} = 2\pi g_{\rm s} N_{\rm c}\,. \tag{2.4}$$

The background D3-brane solution also has a (constant) dilaton and a Ramond-Ramond field, whose precise form are not needed in the following.

Introducing $N_{\rm f}$ D7-branes into the geometry above corresponds to coupling $N_{\rm f}$ fundamental hypermultiplets to the original SYM theory [17]. Before the decoupling limit, the branes are oriented in the following array:

$$\begin{array}{lcccccccccc} & 0 & 1 & 2 & 3 & 4 & 5 & 6 & 7 & 8 & 9 \\ \text{D3:} & \times & \times & \times & \times & & & & & & \\ \text{D7:} & \times & \times & \times & & \times & \times & \times & \times & \times & \times \end{array} \tag{2.5}$$

This configuration is supersymmetric at zero temperature, which ensures stability of the system. After the decoupling limit, the D7 branes wrap an S^3 inside the S^5 of the background geometry. Adapting the S^5 coordinates to this embedding, we write

$$d\Omega_5^2 = d\theta^2 + \sin^2\theta\, d\Omega_3^2 + \cos^2\theta\, d\phi^2 \tag{2.6}$$

[3]Note that we are using the standard D-brane convention here which differs from that of the usual quantum field theory literature. As explained in appendix D of [7], $\lambda = \lambda_{\rm QFT}/2$.

JHEP06(2008)052

in (2.1). Defining $\chi = \cos\theta$, we describe the D7-brane embedding as: $\phi = 0$, $\chi = \chi(\rho)$.

The derivation of the equations of motion for the D7-brane profile $\chi(\rho)$ and the gauge field on their worldvolume A_t was discussed in [13]. Here we will review a few salient points and refer the interested reader to [13] for more details. The DBI action of the D7-branes may be written

$$I_{\rm D7} = -N_{\rm f} T_{\rm D7} \int dt\, d^3x\, d\rho\, d\Omega_3 \frac{(u_0\rho)^3}{4} f\tilde{f}(1-\chi^2)\sqrt{1-\chi^2+\rho^2\dot{\chi}^2 - \frac{2\tilde{f}}{f^2}(1-\chi^2)\dot{\tilde{A}}_t^{\,2}}\,, \quad (2.7)$$

where the dot denotes differentiation with respect to ρ and we have introduced the dimensionless gauge field $\tilde{A}_t$ [13]. The asymptotic form is determined by the gauge field's equation of motion (eq. (2.11) in [13]) as

$$\tilde{A}_t = \frac{2\pi\ell_{\rm s}^2}{u_0}\,\mu_{\rm q} - \frac{\tilde{d}}{\rho^2} + \cdots\,, \quad (2.8)$$

where the constant $\mu_{\rm q}$ is the quark chemical potential. The dimensionless constant $\tilde{d}$ is related to the vacuum expectation value of the quark number density operator with

$$n_{\rm q} = \frac{1}{2^{5/2}}\, N_{\rm f} N_{\rm c} \sqrt{\lambda}\, T^3\, \tilde{d}\,. \quad (2.9)$$

The equation of motion for χ (eq. (2.17) in [13]) implies that the D7-brane profile behaves asymptotically as

$$\chi = \frac{m}{\rho} + \frac{c}{\rho^3} + \cdots\,, \quad (2.10)$$

where the dimensionless constants m and c are proportional to the quark mass and condensate, respectively [6, 7]. In particular, $m = \bar{M}/T$ where

$$\bar{M} = \frac{2M_{\rm q}}{\sqrt{\lambda}} = \frac{M_{\rm gap}}{2\pi} \quad (2.11)$$

is (up to a factor) the meson mass gap $M_{\rm gap}$ at zero temperature [18].

As only $\partial_\rho \tilde{A}_t$ enters the action (2.7), $\tilde{d}$ is a conserved integral of motion and gauge field equation (Gauss' law) yields

$$\partial_\rho \tilde{A}_t = 2\tilde{d}\frac{f\sqrt{1-\chi^2+\rho^2\dot{\chi}^2}}{\sqrt{\tilde{f}(1-\chi^2)[\rho^6\tilde{f}^3(1-\chi^2)^3 + 8\tilde{d}^2]}}\,. \quad (2.12)$$

Substituting this expression into the equation of motion for the profile χ then gives

$$\partial_\rho\left[\frac{1}{\sqrt{\Delta}}\frac{\rho^5 f\tilde{f}(1-\chi^2)\dot{\chi}}{\sqrt{1-\chi^2+\rho^2\dot{\chi}^2}}\right] = -\frac{1}{\sqrt{\Delta}}\frac{\rho^3 f\tilde{f}\chi}{\sqrt{1-\chi^2+\rho^2\dot{\chi}^2}}\left[3\Delta(1-\chi^2+\rho^2\dot{\chi}^2) - \rho^2\dot{\chi}^2\right]\,. \quad (2.13)$$

where Δ is given by

$$\Delta = \frac{\rho^6\tilde{f}^3(1-\chi^2)^3}{\rho^6\tilde{f}^3(1-\chi^2)^3 + 8\tilde{d}^2}\,. \quad (2.14)$$

JHEP06(2008)052

2.1 Black hole embeddings

A key point for the following analysis is that if $n_q \neq 0$ (i.e., $\tilde{d} \neq 0$) then the only physically consistent embeddings for the D7-branes are black hole embeddings [13, 14]. Simply stated, a nonzero density of quarks is dual to a worldvolume electric field, i.e., a nonvanishing $\dot{\tilde{A}}_t$. In turn, this electric field can be interpreted as a finite number of (fundamental) strings dissolved in the probe D7-branes. Since these strings cannot simply terminate, it is not possible for the D7-branes to close off smoothly above the horizon.

Of course, the defining feature of the black hole embeddings is that the probe D7-branes reach the event horizon at $\rho = 1$. We can only solve the profile's equation of motion (2.13) using numerical techniques. Generally we integrate out from the horizon with the following boundary conditions

$$\chi(\rho = 1) = \chi_0\,, \quad \partial_\rho \chi(\rho = 1) = 0\,. \tag{2.15}$$

The series expansion of χ around $\rho = 1$ takes the form[4]

$$\chi = \chi_0 - \frac{3\chi_0(1-\chi_0^2)^3}{4(\tilde{d}^2 + (1-\chi_0^2)^3)}(\rho-1)^2(2-\rho) + O((\rho-1)^4)\,. \tag{2.16}$$

Thus as χ_0 approaches 1 (from below) with $\tilde{d}$ fixed, the profile develops a long narrow throat extending out from $\rho = 1$ — as illustrated in figure 3.

The black hole embeddings were so named because the induced geometry on the D7-brane worldvolume is a black hole geometry. The area of the induced horizon, which is proportional to $(1-\chi_0^2)^{3/2}$, controls the lifetime of excitations on the brane [9]. As discussed below, tuning χ_0 close to 1 will allow us to produce long-lived quasiparticles. However, in the following, we will want to compare the lifetimes of various quasiparticles while keeping the quark mass fixed. Recall that the latter is determined from the asymptotic form of the profile (2.10) at large ρ. Implicitly then with our numerical approach, the constants m and c in (2.10) are functions of both χ_0 and $\tilde{d}$. Hence adding the parameter $\tilde{d}$ is the key to allowing us to vary χ_0 (i.e., the quasiparticle lifetimes) while holding m (i.e., the quark mass) fixed.

We note that the zero-temperature limit of these configurations is a subtle one [19].

2.2 Minkowski embeddings

We comment briefly on Minkowski embeddings with $\tilde{d} = 0$ with reference to the limiting velocity discussed in the introduction. To describe these embeddings, we make the following coordinate transformation [7]

$$\rho^2 = r^2 + R^2\,, \quad \chi = R/\rho\,, \tag{2.17}$$

whereby the equation of motion for the profile $R(r)$ becomes

$$\partial_r\left[\frac{r^3 f \tilde{f}\,\partial_r R}{\sqrt{1+(\partial_r R)^2}}\right] = \frac{8\,r^3 R}{(r^2+R^2)^5}\sqrt{1+(\partial_r R)^2} \tag{2.18}$$

[4] In the numerics, we used this expansion to specify the boundary conditions slightly away from $\rho = 1$.

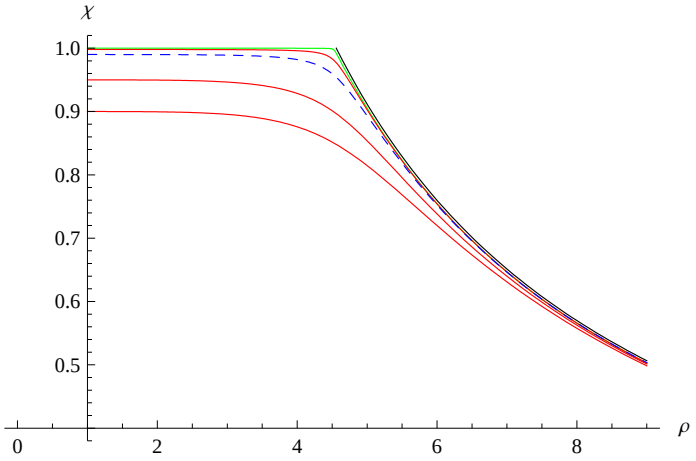

Figure 3: The profile χ as a function of ρ for different values of $\chi_0, \tilde{d}$ with fixed $m = 4.56$. To keep m fixed, $\tilde{d}$ is decreased as χ_0 increases . The black line represents the profile for the corresponding Minkowski embedding with $\tilde{d} = 0$.

where f and $\tilde{f}$ are defined as in (2.2) but now expressed in terms of r and R using (2.17). The boundary conditions specified at $r = 0$ (i.e., $\chi = 1$) are: $R = R_0, \partial_r R = 0$ with $R_0 > 1$. Near the axis $r = 0$, the embedding has an expansion.

$$R = R_0 + \frac{r^2}{R_0(R_0^8 - 1)} + \frac{5R_0^{16} + 5R_0^8 - 3}{3R_0^3(R_0^8 - 1)^3}\, r^4 + O(r^6)\,, \tag{2.19}$$

which, as expected, clearly illustrates that $r = 0$ is the point of closest approach between the D7-brane and the horizon. As commented above, the meson excitations on the Minkowski embeddings were found to approach a limiting velocity at large momentum [7]. This velocity is given by

$$v_{\rm lim} = \sqrt{-\frac{g_{tt}}{g_{xx}}}\bigg|_{\rho=\rho_{\rm min}} = \frac{f}{\tilde{f}}\bigg|_{r=0} = \frac{1 - 1/R_0^4}{1 + 1/R_0^4}\,. \tag{2.20}$$

3. Meson spectral functions

A fruitful application of gauge/gravity duality techniques has proven to be the study of thermal properties of the strongly coupled gauge theories through their finite-temperature correlation functions [20]. In a holographic framework, the spectral functions are typically easier to compute than the full correlators and the poles (and associated residues) of the correlators are still reflected in the corresponding spectral functions. According to the holographic dictionary, the poles are determined by the quasinormal spectrum of a dual bulk field fluctuations, whose study is a technically challenging problem [21] — we begin to address these calculations in sections 4 and 5. In contrast, the spectral function is given by the imaginary part of the retarded correlator,

$$\mathfrak{A}(\omega, \mathbf{q}) = -2\,\mathrm{Im}\, G^R(\omega, \mathbf{q})\,, \tag{3.1}$$

and is determined by appealing to standard calculations of bulk field correlators [22].

JHEP06(2008)052

The retarded correlators have poles in the lower half-plane of complex frequency, which we may assume have the form

$$G^R \sim \frac{A}{\omega - \Omega(q,\alpha) + i\Gamma(q,\alpha)}\,, \tag{3.2}$$

where α represents any additional relevant parameters, e.g., the temperature or quark density. From such a pole, the spectral function receives a contribution

$$\mathfrak{A}(\omega) \sim \frac{2A\Gamma}{(\omega-\Omega)^2+\Gamma^2}\,. \tag{3.3}$$

Thus in the vicinity of $\omega = \Omega$, the spectral function has a peak characterized by a width Γ. A quasiparticle interpretation can be given to the peak if it satisfies the Landau criterion: $\Gamma \ll \Omega$. Hence the masses and lifetimes of quasiparticles can be extracted from the holographic spectral functions.

The spectral function $\mathfrak{A}(\omega)$ also has a characteristic form in the 'high-frequency' limit. This behaviour is determined by the leading short-distance singularity

$$\lim_{(t^2-\mathbf{x}^2)\to 0} \langle \mathcal{O}(t,\mathbf{x})\,\mathcal{O}(0)\rangle = \frac{\mathcal{A}}{|t^2-\mathbf{x}^2|^{\Delta}} + \cdots\,, \tag{3.4}$$

where Δ denotes the dimension of the operator $\mathcal{O}$ and $\mathcal{A}$ is a dimensionless constant. A Fourier transform then leads to the following contribution to the spectral function

$$\mathfrak{A}(\omega) \sim \mathcal{A}\,(\omega^2-q^2)^{\Delta-2}\,. \tag{3.5}$$

Note that this high-frequency tail is Lorentz invariant and shows no indications of a limiting velocity. This should be expected as it describes the very high-energy/short-distance behaviour, which is independent of temperature [9].

In the present study on the gravity side, the D7-brane embeddings extend through the event horizon of the AdS_5 black hole, which describes the theory at finite temperature. As indicated by the name 'black hole embedding', the metric induced on the worldvolume of the D7-branes is itself a black hole. Even though the latter geometry does not obey Einstein's equations, the analysis of the hydrodynamic physics found previously for bulk fields, e.g., [20], is readily transferred to the worldvolume fields on the D7-brane [9] and hence we can examine the spectral function for various mesonic operators following the techniques introduced in [23].

Here, the area of the horizon induced in the worldvolume geometry controls how quickly excitations on the D7-branes are absorbed by the black hole. This absorption rate then determines the lifetime or width of the corresponding quasiparticles in the dual gauge theory. For a black hole embedding with a large horizon area (e.g., the typical situation in the high temperature phase when $\tilde{d} = 0$), one expects to find that $\Gamma \sim \Omega$ [10]. Further the corresponding spectral functions are essentially featureless beyond exhibiting the characteristic high-frequency tail (3.5). However, following the discussion in the previous section, by tuning χ_0 close to 1, the horizon area and consequently the quasiparticle widths shrink. Hence this tuning can bring us into a regime where the spectral functions display distinct

JHEP06(2008)052

peaks with $\Gamma \ll \Omega$ [15]. We re-iterate that having the freedom to independently tune both $\tilde{d}$ and χ_0 is the key to producing these small widths while holding m (i.e., the quark mass) fixed.

In the following, we calculate the spectral densities for the flavour current J^μ which is dual to the worldvolume gauge field A_μ on the supergravity side [13]. These calculations are a simple extension to finite spatial momentum of the spectral function calculations appearing in [15]. We begin by writing the full gauge field as[5]

$$\hat{A}_\mu(\rho, \mathbf{x}) = \delta^t_\mu \, \tilde{A}_t(\rho) + A_\mu(\rho, \mathbf{x}) \,. \tag{3.6}$$

Here $\tilde{A}_t$ denotes the background gauge field (2.12) producing the finite quark density, while A_μ denotes a fluctuation. For simplicity, we assume here that A_μ only depends on ρ and the Minkowski coordinates (and not the internal coordinates on the S^3). To determine the linearized equations of motion for the fluctuations, we expand the DBI action to quadratic order. The resulting gauge field lagrangian is

$$\mathcal{L} = -\frac{1}{4}\sqrt{|\mathcal{G}|}\left[\mathcal{G}^{\mu\alpha}\mathcal{G}^{\beta\gamma}F_{\alpha\beta}F_{\gamma\mu} - \frac{1}{2}\mathcal{G}^{\mu\nu}\mathcal{G}^{\sigma\gamma}F_{\mu\nu}F_{\sigma\gamma}\right] , \tag{3.7}$$

where $\mathcal{G} = g + \tilde{F}$ being the sum of the background metric and background electromagnetic field. Note that the last term does not vanish since $\mathcal{G}$ is no longer a symmetric matrix in general — see comments below, however. The linearized equations of motion for A are then

$$\partial_\nu \left(\sqrt{|\mathcal{G}|}\left[\mathcal{G}^{\nu\mu}\mathcal{G}^{\sigma\gamma} + \frac{1}{2}\mathcal{G}^{[\nu\sigma]}\mathcal{G}^{\mu\gamma}\right] F_{\mu\gamma}\right) = 0 \,. \tag{3.8}$$

Next we consider the Fourier transform of A_μ

$$A_\mu(\rho, \mathbf{x}) = \int \frac{d^4k}{(2\pi)^4} e^{i\mathbf{k}\cdot\mathbf{x}} A_\mu(\rho, \mathbf{k}) \,. \tag{3.9}$$

If we restrict the momentum vector to $(\omega, q, 0, 0)$, the components of the electric field are given by

$$E_x = \omega A_x + q A_0 \,, \qquad E_{y,z} = \omega A_{y,z} \,. \tag{3.10}$$

In the analysis which follows in this section, we will focus on the transverse fields $E_{y,z}$ both of which we will denote by E_T. The analysis for the longitudinal component E_x is more involved on two counts. First, it is only for this mode that the second term in the lagrangian (3.7) contributes to the equation of motion. The second complication is that, in fact, the quadratic lagrangian above is inadequate to describe these modes. This is because with the background field $\tilde{F}_{\rho t}$, these longitudinal modes mix with the scalar fluctuations $\delta\theta$. Hence we leave the complete analysis of these coupled modes for the future.[6]

The linearized equation of motion for E_T can be written as

$$\partial_\rho(F\partial_\rho E_T) + G\left(\mathfrak{w}^2\frac{\tilde{f}^2}{\Delta f^2} - \mathfrak{q}^2\right) E_T = 0 \tag{3.11}$$

[5]Implicitly we are working with the dimensionless gauge field scaled as in [13].

[6]These complications are not evident from the analysis in [15] due to simplifications at $\mathfrak{q} = 0$, for e.g., $\delta\theta$ only mixes with A_0.

JHEP06(2008)052

with

$$F = \frac{\rho^3 f}{\sqrt{\Delta}} \frac{(1-\chi^2)^2}{\sqrt{1-\chi^2+\rho^2\chi'^2}}\,, \quad G = \frac{8\sqrt{\Delta}}{\rho}\frac{f}{\tilde{f}}\sqrt{1-\chi^2+\rho^2\chi'^2}(1-\chi^2)\,. \tag{3.12}$$

Here we have also introduced $\mathfrak{w} \equiv \omega/(2\pi T)$ and $\mathfrak{q} \equiv q/(2\pi T)$. Further recall that Δ is defined in (2.14) and goes to unity when $\tilde{d} = 0$. The retarded Green function for E_T is given by

$$G^R = \frac{N_f N_c T^2}{8}\left[\frac{F}{\omega^2}\frac{\partial_\rho E_T}{E_T}\right]_{\rho\to\infty}\,. \tag{3.13}$$

Now the spectral function is defined as

$$\mathfrak{A}(\omega,k) = -2\,\omega^2\,\mathrm{Im}G^R\,, \tag{3.14}$$

where the extra factor of ω^2 is introduced to produce the spectral function for $A_{y,z}$ — compare to (3.1). Defining

$$\mathfrak{F} = \frac{F}{\mathfrak{w}^2}\frac{\partial_\rho E_T}{E_T}\,, \tag{3.15}$$

it follows from (3.11) that

$$\partial_\rho \mathfrak{F} + \frac{\mathfrak{w}^2}{F}\mathfrak{F}^2 + G\left(\frac{\tilde{f}^2}{\Delta f^2} - \frac{\mathfrak{q}^2}{\mathfrak{w}^2}\right) = 0\,. \tag{3.16}$$

Thus we have

$$\mathfrak{A}(\omega,q) = -\frac{N_f N_c T^2}{4}\,\mathfrak{w}^2\,\mathrm{Im}\mathfrak{F}(\rho\to\infty)\,. \tag{3.17}$$

We solved the above equation numerically taking $E_T(\rho) = (\rho-1)^{-i\mathfrak{w}}e(\rho)$ where $e(\rho)$ is regular at the horizon with the boundary conditions: $e(1) = 1$, $\partial_\rho e(1) = i\mathfrak{w}/2$. This implies $\mathfrak{F}(1) = -4i\sqrt{(1-\chi_0^2)^3+\tilde{d}^2}/\mathfrak{w}$.

Figure 4 illustrates[7] the behaviour of the spectral functions at $\mathfrak{q} = 0$ – this is reproducing the results given in [15]. As discussed above, to construct the background D7-brane embedding, we are varying the variables χ_0 and $\tilde{d}$ while keeping fixed the asymptotic mass (or m). For the cases illustrated in figure 4, we fixed $m = 4.56$ (to within about 0.25% accuracy). These examples explicitly show that as the quark density or induced horizon area increases, the widths of the quasiparticles increases while their positions remains essentially fixed. The figure also shows the positions of the corresponding mesons on the Minkowski embedding with $m = 4.56$ (and $\tilde{d} = 0$) — these masses were determined numerically, as described in [7].

3.1 Dispersion relations

Now to study the dispersion relations, we consider the spectral functions with finite spatial momentum $\mathfrak{q}$. We focus our attention on the first few peaks as these lowest lying resonances are the most prominent at $\mathfrak{q} = 0$. At least for a certain range of $\mathfrak{q}$, the spectral functions

[7] In all our plots in the following, the spectral function $\mathfrak{A}$ is in units of $\frac{N_f N_c T^2}{4}$.

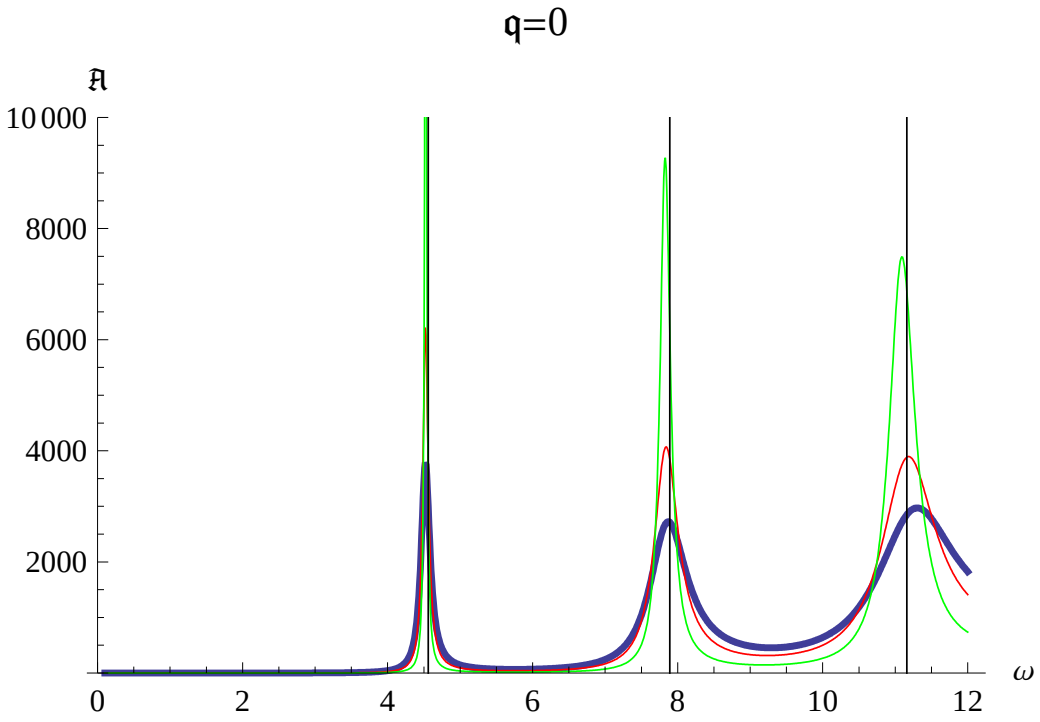

Figure 4: Spectral functions for $m = 4.56$ and $\mathfrak{q} = 0$. The vertical black lines correspond the δ-functions appearing for the Minkowski embedding. The latter appear above at $\mathfrak{w} = 4.56$, 7.89, 11.16, respectively. The green line is for $\tilde{d} = 0.06, \chi_0 = 0.99755$, red for $\tilde{d} = 0.15, \chi_0 = 0.99394$ and blue for $\tilde{d} = 0.25, \chi_0 = 0.99$.

allow us to reconstruct both $\Omega(\mathfrak{q})$ and $\Gamma(\mathfrak{q})$ for these quasiparticles. As might be expected, we will find that beyond a certain $\mathfrak{q}_{\rm crit}$, the corresponding poles (3.2) have moved too far away from the real axis to allow us to identify individual resonances in the spectral functions. We will also be able to estimate the residue $A(\mathfrak{q})$ in the regime $\mathfrak{q} < \mathfrak{q}_{\rm crit}$.

Figure 5 illustrates the typical behaviour of a spectral function as the momentum is increased. In general, one can observe that the quasiparticle peaks are moving to larger values of $\mathfrak{w}$ as $\mathfrak{q}$ increases. Similarly, one would say that increasing $\mathfrak{q}$ causes the individual peaks to become diminished while the background increases. In particular, the high frequency tail (3.5) in the present case is

$$\mathfrak{A}(\mathfrak{w}) = 4\pi\,(\mathfrak{w}^2 - \mathfrak{q}^2) \tag{3.18}$$

with $\Delta = 3$ [9]. In the figure 5, we see that fairly quickly as the momentum is increased, the spectral function becomes well modeled by this tail alone. In fact in the last two plots with $\mathfrak{q} = 100$ and 140, the rise in the spectral function cannot be distinguished from this tail at the scale used there.

Energies, $\Omega(\mathfrak{q})$: to make our discussion more quantitative, we followed the positions $\Omega_i(\mathfrak{q})$ of the (first few) peaks as $\mathfrak{q}$ increases for three different limiting velocities. The three cases are summarized in the following table: The columns labelled Ω_0 and Γ_0 in table 1

JHEP06(2008)052

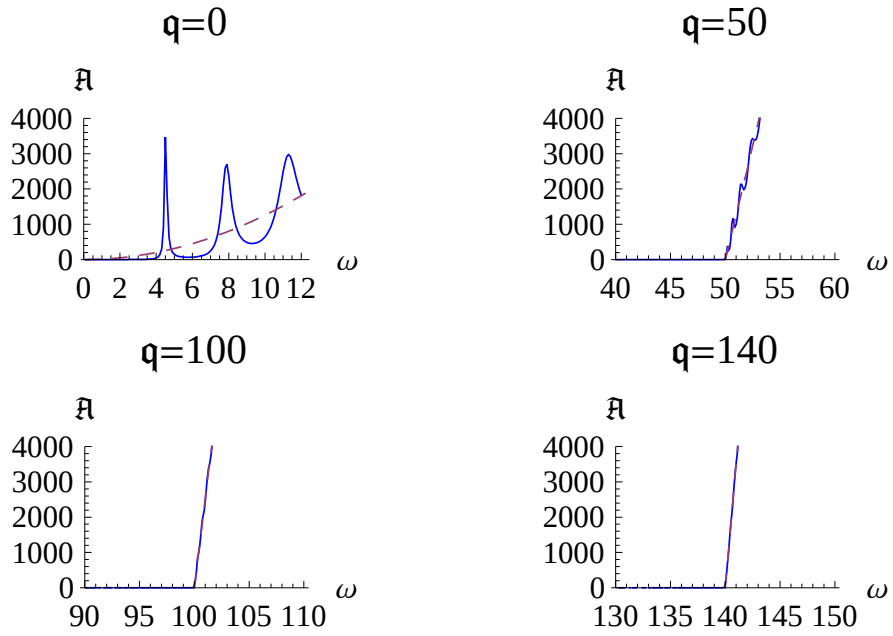

Figure 5: Spectral function versus $\mathfrak{w}$ with $\tilde{d} = 0.25, \chi_0 = 0.99, m = 4.56$ and increasing $\mathfrak{q}$, as indicated. There are no visible peaks above $\mathfrak{q} = 100$. In each plot, the dashed grey line indicates the high frequency tail (3.18) for $\mathfrak{w} \geq \mathfrak{q}$.

	$v_{\rm lim}$	m	$\tilde{d}$	χ_0	Ω_0	Γ_0
I	0.995	4.56	0.25	0.99	4.52	0.072
II	0.651	1.50	0.0005	0.9995	1.37	0.002
III	0.343	1.32	0.0001	0.99975	1.03	0.001

Table 1: Parameters for cases I, II, III.

indicate the position and width of the first peak at $\mathfrak{q} = 0$, respectively, for each case. In each of these cases, we chose $\Gamma_0/\Omega_0 \ll 1$ as this allowed us to follow the first few peaks to much higher momenta. As we will see below, if one begins with broader peaks at $\mathfrak{q} = 0$ then they dissipate more quickly as $\mathfrak{q}$ is increased. As described above at (3.3), the positions of such the peaks[8] $\Omega_i(\mathfrak{q})$ should correspond to the real part of the position of a pole in the corresponding retarded correlator.[9]

The resulting plots of $\Omega_i(\mathfrak{q})$ for these three examples are displayed in figure 6. Note that figure 6 contains two plots which differ primarily in the horizontal scale for $\mathfrak{q}$ because while the peaks could be followed out to $\mathfrak{q} \approx 100$ for case I ($v_{\rm lim} = .995$), they disappeared around $\mathfrak{q} \approx 10$ in the last two cases — see discussion below. In all three cases, the curves

[8] In the following, the subscript is $i = 1, 2, 3$ to denote the first three resonances in the spectral function. Further we identify the position of the resonance with the condition $\partial_{\mathfrak{w}} \mathfrak{A} = 0$ here.

[9] In the following discussion, we denote the position of the poles in the complex $\mathfrak{w}$-plane as $\Omega - i\Gamma$. Hence this usage differs from that in (3.2) or (3.3) by a factor of $2\pi T$.

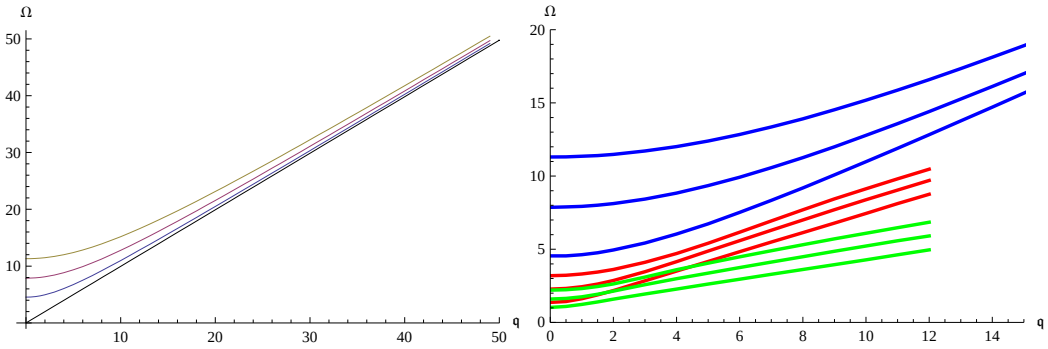

Figure 6: The plot on the left shows the positions of the first three peaks for case I (see table (1)) as a function of $\mathfrak{q}$. Within our accuracy, these curves all asymptote to roughly $\mathfrak{w} = 0.995\mathfrak{q}$, which corresponds to the black line. The plot on the right displays similar dispersion curves for all three cases. The blue, red and green lines correspond to cases I, II and III, respectively.

$\Omega_i(\mathfrak{q})$ appear asymptote to the straight-line form:

$$\Omega_i(\mathfrak{q}) = v_{\rm lim}\,\mathfrak{q} + a_i + O(1/\mathfrak{q}) \tag{3.19}$$

found analytically for the Minkowski embeddings in [12]. Further, as is implicit in our notation, the asymptotic value of the slope $\partial_{\mathfrak{q}}\Omega_i$ matches very well the limiting velocity $v_{\rm lim}$ calculated from the corresponding Minkowski embedding with the same value of m. For $v_{\rm lim} = 0.995$, this is best illustrated in the left panel of figure 6. Figure 7 shows the first peak for the three different cases fit with a straight asymptote with slope $v_{\rm lim}$, as given in (1). This figure makes clear that the two cases with slower limiting velocities approach their asymptotic behaviour (3.19) more quickly. We should comment that while the limiting velocities in (1) gave a good fit to the asymptotic behaviour of these curves, the accuracy of our numerical calculations was limited. The numerical error is estimated as follows: Using $v_{\rm lim} \approx \frac{R_0^4-1}{R_0^4+1}$, we have $\Delta v_{\rm lim} = 8\Delta R_0 \frac{R_0^3}{R_0^8-1} v_{\rm lim}$. Using $\Delta R_0 = \pm 0.01$, this gives $\Delta v_{\rm lim} \approx \pm 0.00004, \pm 0.008, \pm 0.01$ for $v_{\rm lim} = 0.995, 0.651, 0.343$ respectively. Hence we are being slightly extravagant in quoting three significant figures for the latter two cases. We also note that we found that the constants a_i did not seem to match well with the analytic expressions given in [12] for the Minkowski embeddings.

Widths, $\Gamma(\mathfrak{q})$: next we wish to examine how the widths of the quasiparticles evolve with increasing momentum. For this purpose, we list four new trial cases in table 2. Note that the initial widths Γ_0 are tuned to be roughly equal in cases IV, V and VI, which were also chosen to match the same values of $v_{\rm lim}$ as appeared in cases I, II and III in table (1). We have also chosen case VII with $v_{\rm lim} = 0.651$ but tuned so that the ratio Γ_0/Ω_0 is roughly the same as in case IV with $v_{\rm lim} = 0.995$.

As described at (3.3), near the location of an isolated peak in the spectral function, we expect that the spectral function can be approximated as

$$\mathfrak{K} \approx \frac{2A\Gamma}{(\mathfrak{w}-\Omega)^2 + \Gamma^2}\,. \tag{3.20}$$

JHEP06(2008)052

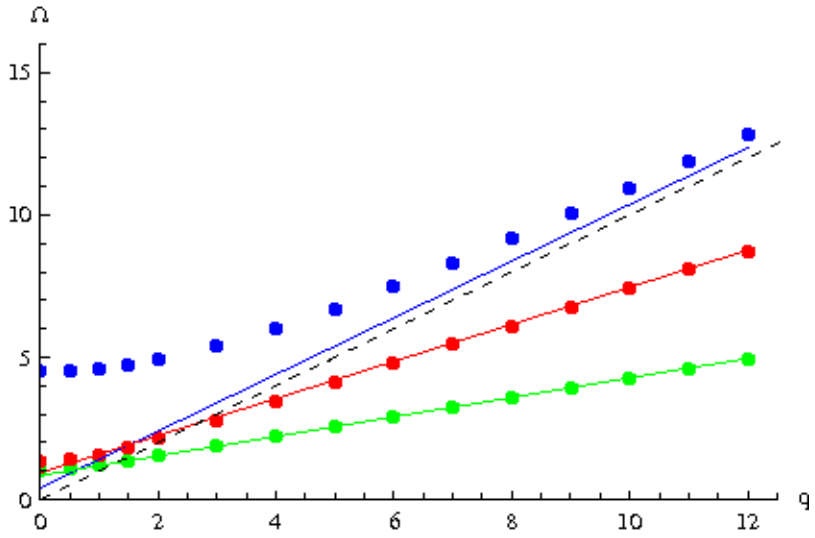

Figure 7: The points above correspond to positions of the first peak from the spectral function for each of the cases in table (1). The corresponding straight lines, which match the asymptotic behaviour in each case, have slopes $v_{\rm lim} = 0.995,\ 0.651$ and 0.343, respectively. The dashed black line has slope one, corresponding to null four-momenta: $\Omega^2 - \mathfrak{q}^2 = 0$.

	$v_{\rm lim}$	m	$\tilde{d}$	χ_0	Ω_0	Γ_0
IV	0.995	4.56	0.15	0.99394	4.52	0.044
V	0.651	1.50	0.01	0.99	1.37	0.04
VI	0.343	1.32	0.0033	0.991	1.03	0.042
VII	0.651	1.50	0.004	0.996	1.37	0.015

Table 2: Parameters for cases IV, V, VI, VII.

From this form, we can derive the following expression for the width of the peak (i.e., the imaginary part in the position of the corresponding pole):

$$\Gamma \approx \sqrt{-2\frac{\mathfrak{K}}{\mathfrak{K}''}}\Bigg|_{\mathfrak{w}=\Omega}, \tag{3.21}$$

where $'$ denotes differentiation with respect to $\mathfrak{w}$. In the above expression, we define $\mathfrak{w} = \Omega$ as the point where $\partial_{\mathfrak{w}}\mathfrak{K} = 0$. The results for the width of the first peak as given by this formula are shown in figure 9 (for each of the four cases in table (2)). Note that each of these curves shows a dramatic increase in Γ as $\mathfrak{q}$ increases from zero. This gives the first hint that we should find a certain maximum value of $\mathfrak{q}$ beyond which the quasiparticles do not exist. Certainly this is observed, e.g., in figure 5 where the peaks in the spectral function are simply washed out at large $\mathfrak{q}$.

Note however, that if the spectral function contains a significant background contribution near $\mathfrak{w} = \Omega$, then the above formula (3.21) will tend to overestimate the true value of Γ. In particular, we can seek to improve the approximate form of the spectral function (3.20)

JHEP06(2008)052

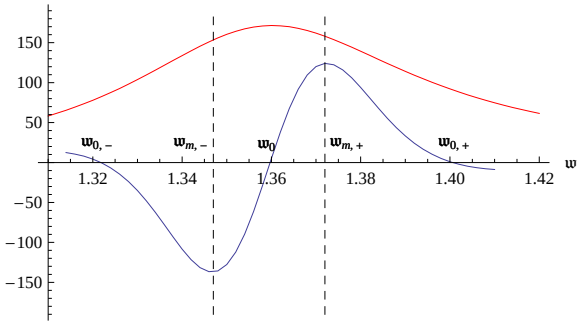

Figure 8: A plot of the first peak in $\mathfrak{R}$ (red) and the corresponding $\partial^3_{\mathfrak{w}}\mathfrak{R}$ (blue) for case V with $\mathfrak{q} = 0$. This illustrates the positions of the frequencies $\mathfrak{w}_0$, $\mathfrak{w}_{0,\pm}$ and $\mathfrak{w}_{m,\pm}$ discussed in the text. $\partial^3_{\mathfrak{w}}\mathfrak{R}$ has be scaled by 1/200 in this plot.

in the vicinity of one of the peaks by also including the high frequency tail (3.18)

$$\mathfrak{R} \approx \frac{2A\Gamma}{(\mathfrak{w}-\Omega)^2+\Gamma^2} + 4\pi(\mathfrak{w}^2-\mathfrak{q}^2)\,. \tag{3.22}$$

Now we observe, however, that by taking the third derivative, $\partial^3_{\mathfrak{w}}\mathfrak{R}$, the background introduced by the tail in the above expression will be eliminated. Further the resulting expression will have zeros at $\mathfrak{w}_0 \equiv \Omega$ and $\mathfrak{w}_{0,\pm} \equiv \Omega \pm \Gamma$ and so in principle, the zeros of $\partial^3_{\mathfrak{w}}\mathfrak{R}$ can be used to determine Γ. However, rather than working directly with these zeros, we note that there are also a maximum and a minimum to either side of the central zero at Ω. A straightforward calculation shows that these extrema occur at

$$\mathfrak{w}_{m,\pm} \equiv \Omega \pm \delta\ \Gamma \qquad \text{with}\quad \delta = \sqrt{1-\frac{2}{\sqrt{5}}} \simeq 0.3249\,. \tag{3.23}$$

The above features are illustrated in figure 8. We can use these expressions to estimate both the width of a given peak but also an error because our form (3.20) is not perfect. In particular, we have

$$\bar{\Gamma} = \frac{\mathfrak{w}_{m,+}-\mathfrak{w}_{m,-}}{2\delta} \qquad \Delta\Gamma = \frac{1}{2\delta}\left(\mathfrak{w}_{m,+}+\mathfrak{w}_{m,-}-2\mathfrak{w}_0\right)\,. \tag{3.24}$$

The results for the width using these expressions are also shown in figure 9. One can note that again there is dramatic rise in Γ as $\mathfrak{q}$ increases, again hinting at a $\mathfrak{q}_{\rm crit}$. These results for $\bar{\Gamma}$ seem to agree fairly well with those originally derived with (3.21). However, this agreement is not as good for larger values of $\mathfrak{q}$ where the quasiparticle peaks are washed out and $\Delta\Gamma$ is larger. In particular, as might be expected, (3.21) tends to give a larger width than (3.24) in this regime.

In fact, the increase in the widths is only one of three effects leading to the dissolution of the quasiparticle peaks in the spectral functions. The second effect which we consider here is the decreasing separation of neighbouring peaks or poles along the real axis. As

JHEP06(2008)052

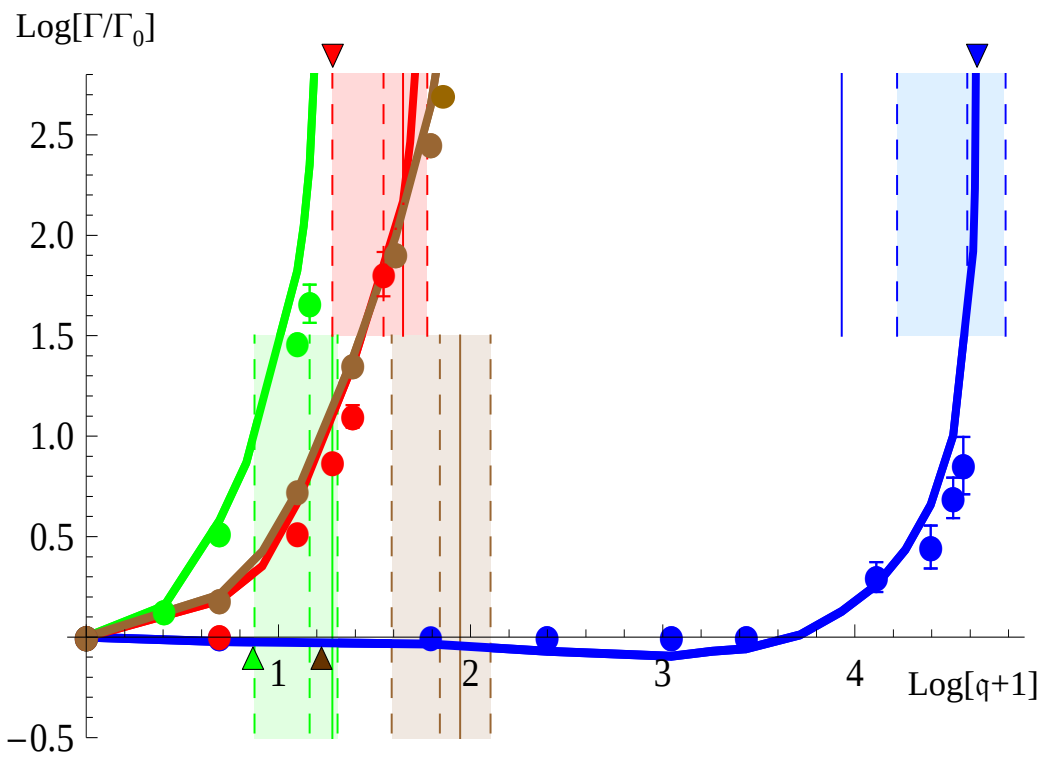

Figure 9: $\log(\Gamma/\Gamma_{\mathfrak{q}=0})$ vs $\log(\mathfrak{q}+1)$. The continuous curves were obtained using the spectral plots and formula (3.21). The blue, red, green and brown lines correspond to cases IV, V, VI and VII in table (2), respectively. The points with 'error bars' were obtained using (3.24). The vertical dashed lines within the shaded regions indicate the location where the zero $\mathfrak{w}_{m,+}$ in $\partial^3_{\mathfrak{w}}\mathfrak{K}$ is lifted. The left extreme of the shaded regions correspond to $\mathfrak{q}$ when $\mathfrak{w}_{0+}$ is lifted while the right extreme corresponds to $\mathfrak{q}$ when $\mathfrak{w}_0$ is lifted. The solid vertical lines indicate where a point of inflexion occurs in the effective potential, as described in section 4. The arrows indicate where $\mathfrak{q} = \Omega$.

shown in figure 9, one finds that $\Delta\Gamma$ from (3.24) also increases with increasing $\mathfrak{q}$. This is indicating a greater asymmetry in $\partial^3_{\mathfrak{w}}\mathfrak{K}$ around the position of the peak $\mathfrak{w}_0 \equiv \Omega$. Of course, this is actually indicates that the form (3.22) is becoming a poor approximation for the spectral function in the vicinity of the peaks. Essentially the problem is that assuming that the peaks are isolated is incorrect in this regime. To illustrate this behaviour for case VI, we show the ratio of the separation of the first two peaks to the sum of their widths in figure 10. From our plot, we see that this ratio approaches one indicating that this first peak is no longer isolated from the other quasiparticle peaks at higher $\mathfrak{w}$. The same behavior is observed for the other cases. For cases IV, V, VII we have for $\mathfrak{q} = 0$, the ratio $\log(\Omega_2 - \Omega_1)/(\bar{\Gamma}_2 + \bar{\Gamma}_1) = 2.54, 1.54, 2.36$ respectively while the ratio near $\mathfrak{q}$ where $\mathfrak{w}_{m,+}$ becomes a point of inflection becomes $.28(\mathfrak{q} = 90), .40(\mathfrak{q} = 3.6), .36(\mathfrak{q} = 5)$ in the respective cases.

JHEP06(2008)052

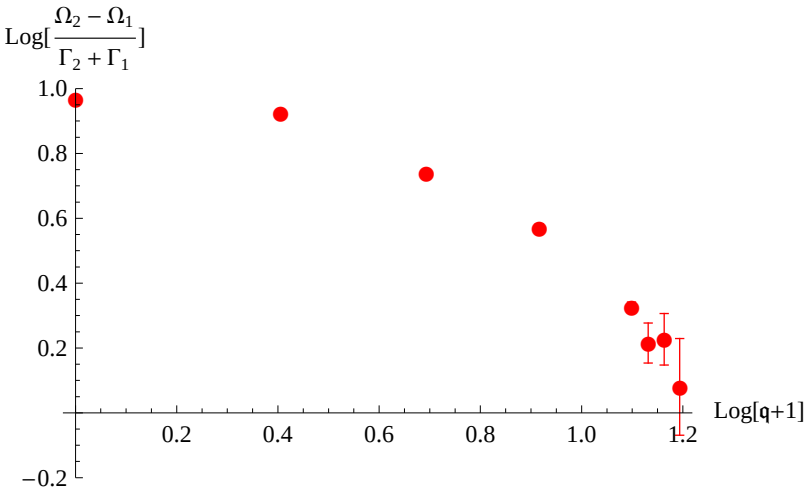

Figure 10: Plot of $\log(\Omega_2-\Omega_1)/(\Gamma_2+\Gamma_1)$ for case VI. The central values arise from using $\Gamma_{1,2}=\bar{\Gamma}_{1,2}$ while the upper and lower 'error' bars are determined with $\Gamma_{1,2}=\bar{\Gamma}_{1,2}\pm\Delta\Gamma_{1,2}$. The ratio approaches one for larger $\mathfrak{q}$ indicating that these resonances in the spectral function should not be considered to be isolated peaks.

The first peak which we are following then loses its shape due to the encroachment of the neighbouring peaks. The typical development as $\mathfrak{q}$ increases is that first the zero at $\mathfrak{w}_{0,+}$ is lifted. Next the maximum at $\mathfrak{w}_{m,+}$ becomes a point of inflection and then is subsequently lost. Finally, the zero at $\mathfrak{w}_0$ itself lifted when it collides with $\mathfrak{w}_{0,-}$ (and simultaneously with $\mathfrak{w}_{m,-}$). The region where the first peak is losing its shape in this way is indicated with the shading in figure 9 for each of the four cases. This dissolution of the first peak is illustrated in detail for case V in figure 11. As shown, first $\mathfrak{w}_{0,+}$ is lifted around $\mathfrak{q}=2.6$. This is followed by the maximum $\mathfrak{w}_{m,+}$ becoming a point of inflexion around $\mathfrak{q}=3.7$ and finally $\mathfrak{w}_0$ is itself lifted around $\mathfrak{q}=4.9$.

Beyond the point where $\mathfrak{w}_0$ is lifted, there is no (simple) way to use the spectral function to follow the corresponding pole in the thermal correlator and certainly there is no sense in applying the concept of a quasiparticle. One might use the lifting of the zero $\mathfrak{w}_0$ as defining the value $\mathfrak{q}_{\rm crit}$ where the quasiparticles disappear. These momenta for each of the four cases in figure 9 coincides to the extreme right of the corresponding shaded region. We return to these issues in the discussion in section 6.

A clear trend that emerges from figure 9 above is that the value of $\mathfrak{q}_{\rm crit}$ increases with increasing $v_{\rm lim}$. This is already clear in comparing the results for cases IV, V and VI, all of which start with $\Gamma_0\simeq 0.04$. However, while $v_{\rm lim}$ is certainly one parameter that changes between these three cases, another parameter which distinguishes these three cases is Γ_0/Ω_0. The latter increases significantly between these three cases while the limiting velocity is decreasing and one might imagine that if the quasiparticle peaks begin by being less well resolved, they should be washed out more quickly. Hence we also considered case VII for which $v_{\rm lim}=0.651$ and $\Gamma_0/\Omega_0\simeq 0.01$. So here the limiting velocity matches that in case V (for which $\Gamma_0/\Omega_0\simeq 0.03$) but the ratio Γ_0/Ω_0 was tuned to match roughly that in case IV (for which $v_{\rm lim}=0.995$). In figure 9, we see that the width for case VII grows with

JHEP06(2008)052

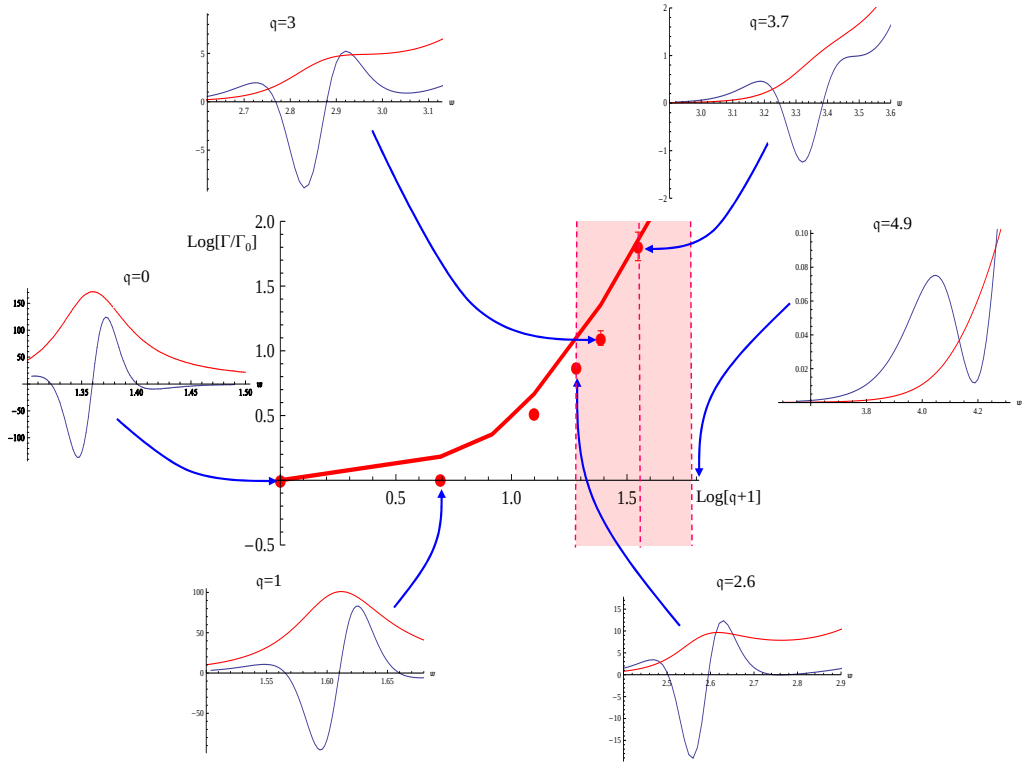

Figure 11: The central plot shows the behaviour of Γ with $\mathfrak{q}$ for case V as in figure 9. For each point in this plot, we also show the corresponding spectral function $\mathfrak{A}$ denoted by red and $\partial^3_{\mathfrak{w}}\mathfrak{A}$ denoted by blue. This typical example illustrates how the peaks lose their form with increasing $\mathfrak{q}$.

$\mathfrak{q}$ in close accord with that for case V. We note though that our estimates of $\mathfrak{q}_{\rm crit}$ for case VII were slightly larger than those of case V. In any event, these results seem to indicate that $v_{\rm lim}$ is the dominant factor in determining critical momentum where the quasiparticles disappear.

For comparative purposes, we also show in figure 12 the ratio of the widths of the first two peaks in case VI, as calculated with (3.24). As the plot shows, the width of the second peak increases more slowly than the first. For instance, $\Gamma_2(\mathfrak{q})/\Gamma_1(\mathfrak{q}) \simeq 4.3$ at $\mathfrak{q} = 0$ but only 1.3 at $\mathfrak{q} = 2.2$. This behaviour is in fact typical for all of the cases which we studied here.

Residues, $A(\mathfrak{q})$: so far our discussion of the quasiparticle peaks has focussed on their energy Ω and the width Γ, which correspond to the real and imaginary parts of the position of a pole in the thermal correlator (3.2). Here we briefly turn to the residue A, as this also determines the size of the peak corresponding to a given pole — e.g., for the canonical shape (3.3), the maximum value of spectral function is: $\mathfrak{A}(\mathfrak{w} = \Omega) = 2A/\Gamma$. Assuming the peaks have this canonical shape, the residue can also be determined in a number

JHEP06(2008)052

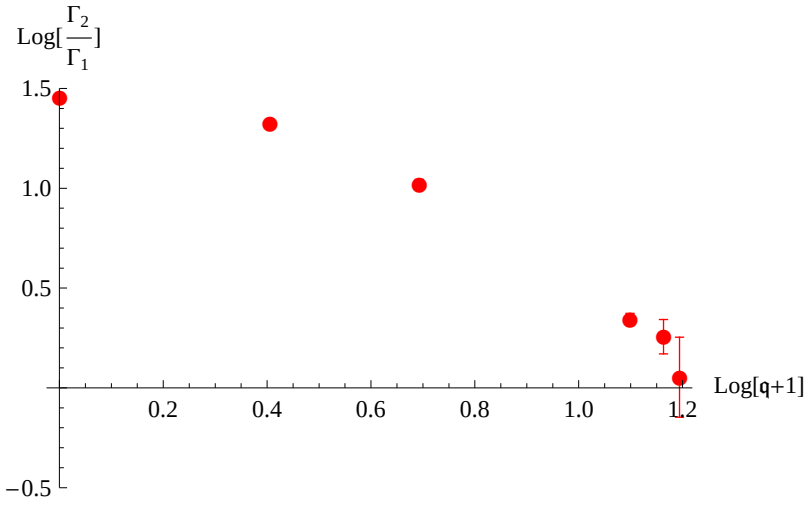

Figure 12: The plot shows $\log(\Gamma_2/\Gamma_1)$ for the first two peaks in case VI. For these two peaks, Γ_0 takes the values $0.042, 0.184$ respectively. The first peak disappears at $\mathfrak{q} \approx 3$ while the second peak disappears at $\mathfrak{q} \approx 2.72$.

of different ways from the spectral functions but we focus on the third derivative of the spectral function following the above discussion for the form given in eq. (3.22). First, we can relate A to the slope of $\partial^3_{\mathfrak{w}} \mathfrak{R}$ at $\mathfrak{w} = \mathfrak{w}_0$:

$$A_1 = \frac{\Gamma^5}{48}\, \partial^4_{\mathfrak{w}} \mathfrak{R}\Big|_{\mathfrak{w}=\mathfrak{w}_0} \,. \tag{3.25}$$

This expression evaluated with $\bar{\Gamma}$ from eq. (3.24) is shown in figure 13 for the four cases in table 2. Alternatively, the residue A can be determined by the value of the extrema at $\mathfrak{w} = \mathfrak{w}_{m,\pm}$:

$$A_{2,\pm} = \pm\frac{\Gamma^4}{48}\, \frac{(1+\delta^2)^4}{\delta(1-\delta^2)}\, \partial^3_{\mathfrak{w}} \mathfrak{R}\Big|_{\mathfrak{w}=\mathfrak{w}_{m,\pm}} \,. \tag{3.26}$$

Our first observation is that the results for all three of these expressions seem to agree quite well. One might also note how similar the results are for cases V and VII, which both have $v_{\rm lim} = 0.651$. The most significant effect apparent in figure 13 is that A decreases quite rapidly as $\mathfrak{q}$ increases. This effect is most dramatic in case IV where the results for A are fit well by an exponential: $A \simeq 140\, \exp[-0.077\, \mathfrak{q}]$. This rapid fall in A with increasing $\mathfrak{q}$ was the third effect which we identified as contributing to the disappearance of the quasiparticle peaks in the spectral function.

4. Quasinormal modes

The basic features of the spectral functions are controlled by the analytic structure of the corresponding retarded correlators in the complex frequency plane. Holographically, these poles correspond to quasinormal modes of excitations in the black hole geometry induced on the D7-brane [22, 24]. Investigating the quasinormal spectrum for the black

JHEP06(2008)052

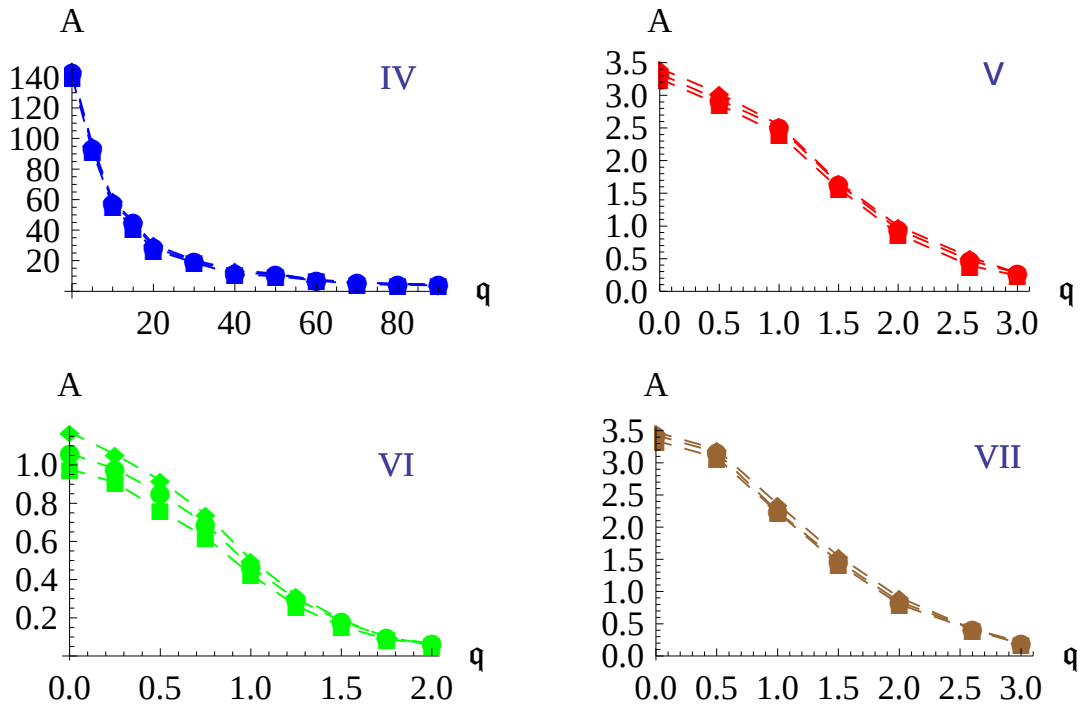

Figure 13: The residue A calculated for the first peak in the four cases given in table 2. The circles correspond to results for A_1 in eq. (3.25), while the squares and diamonds correspond to $A_{2,\pm}$ in (3.26), respectively.

hole embeddings of interest is a technically challenging problem which we intend to pursue elsewhere [25]. However, as described in [9], some qualitative information can be inferred from casting the relevant radial equations of motion in the form of a Schrödinger equation. In particular, one naively expects that the appearance of quasiparticle peaks with $\Gamma \ll \Omega$ in the spectral function would correspond to metastable states supported by a local minimum in the effective potential of the Schrödinger equation. Conversely, the absence of a local minima could be expected to yield the non-existence of quasiparticles. In this section, we apply this kind of qualitative analysis to the transverse vector and pseudoscalar fluctuations of the D7-brane. These calculations allow us to gain some qualitative insight into the quasinormal modes for these fields — see, e.g., [10, 26]. One might be tempted to apply a WKB analysis in this framework to obtain some quantitative results as well, however, as we describe in appendix A, such an approach will not yield reliable results.

Let us begin with (3.11), the equation of motion for the transverse vector, and follow the approach described in appendix of D of [9]. Defining[10] $H_0 = (f^2 F\Delta)/(\tilde{f}^2 G)$ and $E_T = h\psi$, we find that choosing $h = H_0^{1/4}/F^{1/2}$ recasts this equation into

$$-\partial_{R_*}^2 \psi + V\,\psi = \mathfrak{w}^2\,\psi\,, \tag{4.1}$$

[10]Recall that F and G are defined in (3.12) and Δ, in (2.14).

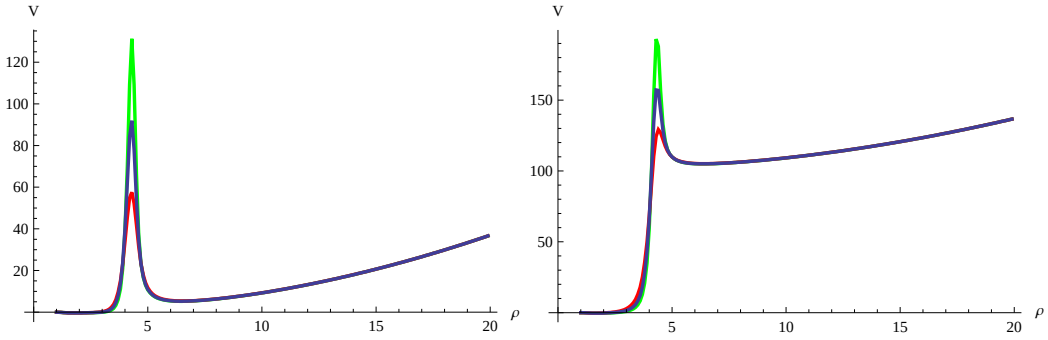

Figure 14: The plot on the left is for V_0 vs ρ for $v_{\rm lim} = 0.995$ and $\tilde{d} = 0.15$ (case IV; green), 0.25 (case I; blue), 0.5 (red). The potential barrier diminishes with increasing $\tilde{d}$. The plot on the right shows the total potential V with $\mathfrak{q} = 10$ for the same range of parameters.

where $R_* \equiv \int_\rho^\infty d\tilde{\rho}/\sqrt{H_0(\tilde{\rho})}$ and the effective potential V is given by

$$\begin{aligned} V &= \frac{f^2}{\tilde{f}^2}\Delta\left[-\frac{1}{G\,h}\partial_\rho(F\partial_\rho h) + \mathfrak{q}^2\right] \\ &= V_0 + \mathfrak{q}^2\ V_1\,. \end{aligned} \tag{4.2}$$

Note that with the above definition for R_*, we have $R_* \to \infty$ at the horizon (i.e., $\rho \to 1$) and $R_* \to 0$ asymptotically (i.e., $\rho \to \infty$). We also note that the simple dependence of the Schrödinger problem on the frequency and wave-number of the mesons. That is, $\mathfrak{w}^2$ plays the role of the effective energy while $\mathfrak{q}^2$ appears as the coefficient of a new term V_1 in the effective potential. Further we observe that in the limit that $\rho \to \infty$, $V_1 \to 1$ and hence in this UV regime, these two contributions can be recombined in the Lorentz invariant form $\mathfrak{w}^2 - \mathfrak{q}^2$.

We begin by illustrating the behaviour of V_0 in figure 14. We might compare this to the corresponding effective potential discussed for the Minkowski embeddings in [18]. Both there and here, the effective potential rises to infinity for large ρ which simply reflects the infinite gravitational potential of the AdS geometry. In the Minkowski case, there is also an infinite barrier at $\rho = R_0$ where the D7-brane embedding ends and so this potential leads to a discrete spectrum of (stable) bound states. As described in section 2.1, the D7-branes of interest here with $\tilde{d}$ have a narrow neck that extends down to the black hole horizon at $\rho = 1$. As a result, the infinite barrier at $\rho = R_0$ above, is reduced to a finite barrier, as illustrated in figure 14. As a result, one's intuition should be that the low lying bound states for the Minkowski problem remain essentially unchanged but they are now only metastable because they will slowly tunnel out through the potential barrier to the horizon. Further as shown in figure 14, as $\tilde{d}$ increases (with m fixed), the height of the potential barrier shrinks and so the decay rate of these metastable states will increase. Of course, for highly excited states with $\mathfrak{w}^2$ above the top of the barrier, the spectrum will be completely changed and in particular, we do not expect to speak in terms of metastable states.

JHEP06(2008)052

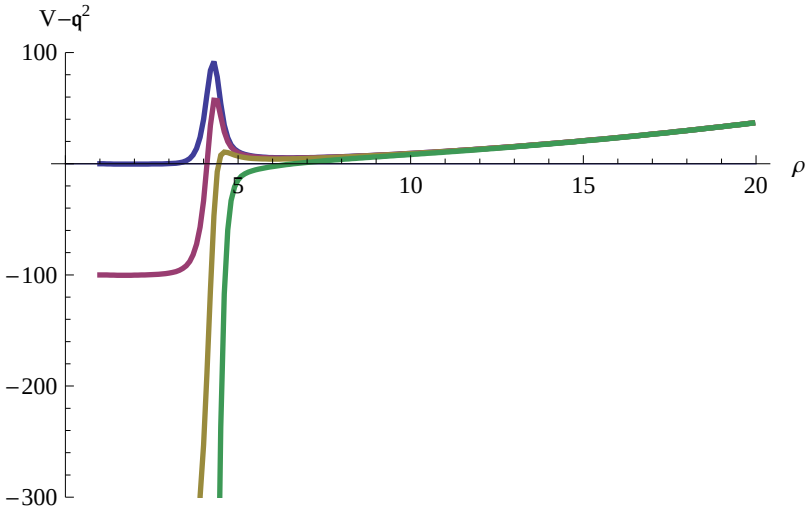

Figure 15: $V - \mathfrak{q}^2$ vs ρ for case I (i.e., $\tilde{d} = 0.25$ and $\chi_0 = 0.99$). The curves correspond to $\mathfrak{q} = 0$ (blue), 10 (pink), 20 (yellow) and 50 (green). As $\mathfrak{q}$ increases the barrier decreases and eventually disappears.

When the meson states also have a finite momentum, we must also account for the contribution $\mathfrak{q}^2 V_1$ to the effective potential. Given the expression in (4.2), one finds that this term raises the effective potential by a finite amount are larger values of ρ. As illustrated on the right in figure 14, while both the local maximum and minimum in the potential are raised, the primary effect of increasing $\mathfrak{q}$ is to raise the minimum relative to the maximum, i.e., the barrier shielding the potential well from the horizon is reduced. This effect is also illustrated in figure 15 where we have plotted $V - \mathfrak{q}^2$ with changing $\mathfrak{q}$ — subtracting $\mathfrak{q}^2$ ensures that the asymptotic form of the resulting curves is fixed, as can be inferred from the discussion below (4.2).

To summarize, recasting the equation of motion in the Schrödinger form (4.1) gives an intuitive picture which yields the following key observations: For small $\mathfrak{q}$, the effective potential has a large barrier, which is responsible for the metastability of the quasiparticles. However, this barrier shrinks with increasing $\mathfrak{q}$ which then explains why the decay rates of the metastable states should increase as $\mathfrak{q}$ increases. Further this barrier actually disappears above some momentum which again points to a critical momentum $\mathfrak{q}_{\rm crit}$ beyond which the quasiparticles disappear.

We can use this analysis to establish a quantitative criterion for this maximum momentum $\mathfrak{q}_{\rm crit}$. Since our intuition is that metastable states exist because of the potential barrier appearing in V, we propose to estimate $\mathfrak{q}_{\rm crit}$ as the value of the momentum at which the barrier disappears and is reduced to a point of inflexion. We have shown these estimates in figure 9 for the three cases described in table (2). It seems that for cases V, VI and VII (with the smaller values of $v_{\rm lim}$), these estimates are well within the region where the peaks are losing their canonical shape and in fact, are quite close to the point where the zero at $\mathfrak{w}_0$ is lifted. The latter was also suggested as a measure of $\mathfrak{q}_{\rm crit}$ in the previous section. For case IV with $v_{\rm lim} = .995$, the result here gives a smaller value of $\mathfrak{q}$ outside of

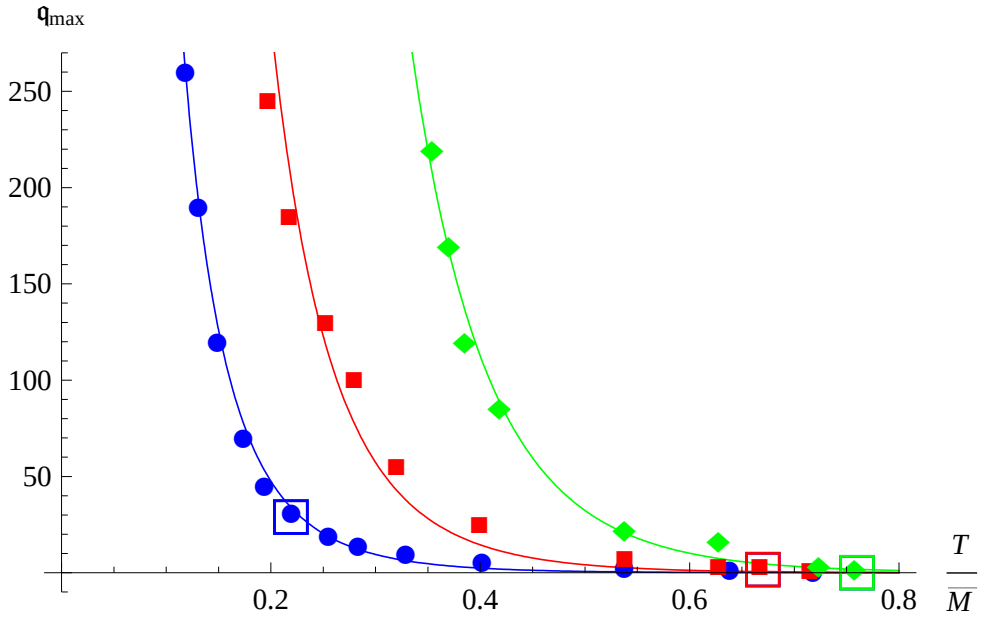

Figure 16: This plot shows $\mathfrak{q}_{\rm crit}$ vs $T/\bar{M}$ for E_T. The blue, red and green points and curves correspond to $\tilde{d} = 0.25$, 0.0005 and 0.0001, respectively. Further the boxes surround the points corresponding to cases I, II and III in table (1). The continuous curves come from fitting the data points with the form $\exp[-8x]/x^2$.

the region where peak is losing its shape and so present calculation seems to underestimate $\mathfrak{q}_{\rm crit}$. However, it still seems to coincide with the onset of the rapid rise in Γ. It seems somewhat surprising though that the widths could still be relatively small after the barrier in the effective Schrödinger potential had disappeared.

In any event, the advantage of the present approach to estimating $\mathfrak{q}_{\rm crit}$ is that it is computationally simple and relatively inexpensive. For example, in figure 16, we used this approach to determine the behaviour of $\mathfrak{q}_{\rm crit}$ as a function of $T/\bar{M}$. As $T/\bar{M}$ essentially fixes $v_{\rm lim}$, these results are again displaying the strong correlation between $\mathfrak{q}_{\rm crit}$ and the limiting speed discussed in the previous section. In figure 16, the continuous curves were constructed by fitting the data points with the form $\exp[-8x]/x^2$. Hence we find in the zero temperature limit, $\mathfrak{q}_{\rm crit} \propto (\bar{M}/T)^2 \to \infty$. Furthermore, in the limit that $\tilde{d} \to 0$ (and hence $\Gamma_0 \to 0$), $\mathfrak{q}_{\rm crit} \to \infty$.

We close this section with a few technical comments. One may have imagined that the decay widths would be calculable in the corresponding Schrödinger problem using a WKB approximation. Such a calculation is outlined in appendix A. However, as also explained there, this approach does not generally yield reliable results. The essential point is that for the WKB approximation to be valid, the change of the momentum over a wavelength must be small compared to the momentum itself. Unfortunately, in the examples considered here, this condition in not met within the barrier making the WKB analysis unreliable.

Finally we comment briefly on the effect on the widths from adding angular momentum on the internal S^3. That is, all of mesons considered up to this point have been singlets

JHEP06(2008)052

under the internal SU(2) × SU(2) global symmetry of the gauge theory — this symmetry is dual to rotations on the D7-brane's internal S^3. However, these states only correspond to the lowest dimension operators in an infinite family of vector operators transforming in the $(\ell/2, \ell/2)$ representation of the internal symmetry [18]. So we wish now to consider states with nonvanishing ℓ. In fact, we will turn to the pseudoscalar mesons at this point since the analysis in this case is somewhat simpler. For non-zero ℓ and $\mathfrak{q}$, A_ρ cannot generally be set to zero [9] which complicates the analysis for the vector. However, adding angular momentum to the pseudoscalar case is straightforward and so we consider this case here. The equation of motion for the pseudoscalars, i.e., fluctuations in ϕ, can be written as

$$\partial_\rho(F\partial_\rho \mathcal{P}) + G\left(\mathfrak{w}^2\frac{\tilde{f}^2}{\Delta f^2} - \mathfrak{q}^2\right)\mathcal{P} + \ell(\ell+2)H\,\mathcal{P} = 0\,, \tag{4.3}$$

where the functions F, G, H are defined as

$$H_0 = \frac{\rho^4 f^2}{8\tilde{f}}\frac{1-\chi^2}{1-\chi^2+\rho^2\chi'^2}\,, \qquad F = \frac{\rho^5 f\tilde{f}\chi^2(1-\chi^2)^2}{\sqrt{\Delta}\sqrt{1-\chi^2+\rho^2\chi'^2}}\,, \tag{4.4}$$

$$H_2 = \Delta\frac{f^2}{\tilde{f}^2}\,, \quad H_3 = \frac{\rho^2 f^2\Delta}{8\tilde{f}(1-\chi^2)}\,, \quad G = \frac{FH_2}{H_0}\,, \quad H = \frac{FH_3}{H_0}\,. \tag{4.5}$$

It can be shown that the effective Schrödinger potential in this case can be written as [9]

$$V = V_0 + \mathfrak{q}^2\,V_1 + \ell(\ell+2)\,V_2 \tag{4.6}$$

$$= -\frac{H_0}{hF}\partial_\rho(F\partial_\rho h) + \mathfrak{q}^2\,H_2 + \ell(\ell+2)\,H_3\,, \tag{4.7}$$

where $h = H_0^{1/4}/F^{1/2}$. Some examples of the effective potential are shown in figure 17. The key feature which one observes from this plot is that introducing $\ell \neq 0$ increases the potential barrier. This is not surprising since the D7-brane embedding has a narrow neck near the horizon, i.e., the S^3 is small, and so this increase reflects an angular momentum barrier for these modes. We also note that the plots of the potential for the vector meson E_T for $\ell = 0$ are almost indistinguishable from those for the pseudoscalar even for non-zero $\mathfrak{q}$. In fact the two potentials differ by less than 1% although their precise functional forms are not identical.

5. Beyond $\mathfrak{q}_{\rm crit}$

As we saw in section 3, the analysis of the spectral functions can only give limited information about the dispersion relations. In particular, when the quasiparticles become too unstable with increasing $\mathfrak{q}$, they no longer contribute characteristic features to the spectral function which would allow us to infer $\Omega(\mathfrak{q})$ and $\Gamma(\mathfrak{q})$. Of course, this simply indicates that the corresponding pole in the thermal correlator (3.2) has moved down in the complex plane, too far from the real axis to strongly influence the spectral function. The behaviour of these poles can be followed to higher momenta in the present holographic framework with a direct analysis of the corresponding quasinormal modes [21, 27, 28]. While we intend

JHEP06(2008)052

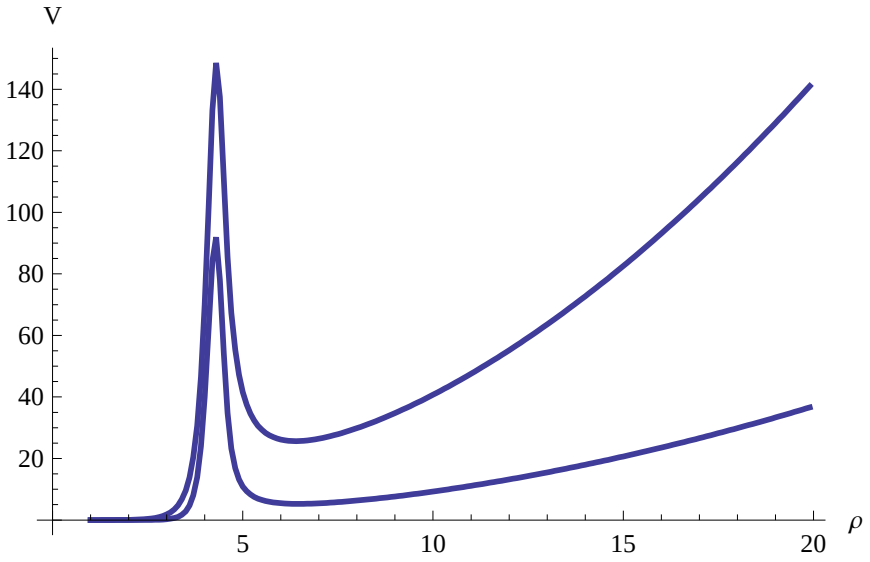

Figure 17: This plot is for the effective Schrödinger potential for the pseudoscalar field with $\ell = 0, 1$ and $\mathfrak{q} = 0$, $d = 0.25$, $\chi_0 = 0.99$. The higher potential is for $\ell = 1$.

to pursue this problem elsewhere [25], here we will attempt to provide some qualitative insight into the behaviour of the poles at higher momentum and also for the higher quasi-normal modes, using the intuitive picture of the effective Schrödinger problem given in the previous section.

Our intuitive picture will also be guided by a comparison with the results for the R currents in $\mathcal{N} = 4$ SYM at finite temperature. That is, we start by considering the behaviour of the transverse vector modes of a Maxwell field in AdS_5. A closely related investigation of the longitudinal vector modes and a massless minimally coupled scalar appeared in [27] and [28], respectively.[11] The relevant equation of motion for the transverse vector modes E_T in AdS_5 can be found in [9, 21] and can be written as

$$\partial_\rho \left(\rho^3 f \partial_\rho E_T\right) + \frac{8}{\rho}\frac{f}{\tilde{f}}\left(\mathfrak{w}^2 \frac{\tilde{f}^2}{f^2} - \mathfrak{q}^2\right) E_T = 0\,, \tag{5.1}$$

where f and $\tilde{f}$ are defined above in (2.2). This equation of motion is equivalent to that of the analogous modes of the D7-brane gauge field (3.11) with $\chi = 0$ and $\tilde{d} = 0$. Hence using the results of section 4, eq. (5.1) is easily recast into the Schrödinger form

$$-\partial^2_{R_*}\psi + V(\rho)\,\psi = \mathfrak{w}^2\psi\,, \tag{5.2}$$

where $R_* = \int_\rho^\infty d\tilde{\rho}/\sqrt{H_0(\tilde{\rho})}$ with $H_0(\rho) = \rho^4 f^2/8\tilde{f}$. The wave-function has been defined as $\psi \equiv E_T/h$ with $h = (8\rho^2\tilde{f})^{-1/4}$ and the effective potential $V(\rho)$ is given by

$$V(\rho) = V_0 + \mathfrak{q}^2\ V_1 = \frac{f^2}{\tilde{f}^2}\left[\frac{3}{32}\,\rho^2\tilde{f} + \frac{5}{8}\,\frac{1}{\rho^2\tilde{f}} + \mathfrak{q}^2\right]\,. \tag{5.3}$$

[11] There is an erroneous claim in [27] that the results for the transverse vector modes should be precisely the same as for that for the massless minimally coupled scalar field given in [28].

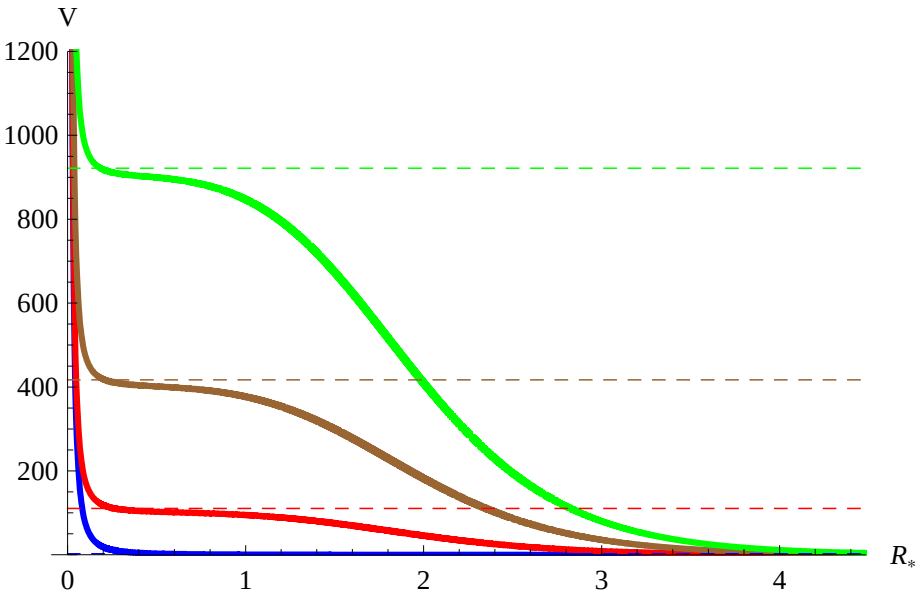

Figure 18: The plot shows $V - \mathfrak{q}^2$ vs R_*. Blue, red, brown and green are for $\mathfrak{q} = 0, 10, 20, 30$ respectively. The dashed lines indicate the lowest eigenfrequency obtained from the spectral function at these $\mathfrak{q}$'s.

Again the effective potential in eq. (4.2) reduces to that above upon setting both χ and $\tilde{d}$ to zero. Figure 18 presents various plots of the effective potential versus the Schrödinger coordinate R_* for various values of $\mathfrak{q}$. In figure 20, we also compare this potential (5.3) for the supergravity vector modes with that for the analogous D7-brane modes for different values of the quark mass and $\tilde{d}$.

As noted above, [27, 28] presented an analysis of quasinormal modes for similar supergravity fields in AdS_5. Here in our preliminary analysis of the transverse vector, we use only the spectral function techniques described in section 3 for the lowest lying modes. The analogue of eq. (3.16) is given here by

$$\partial_\rho \mathfrak{F} + \frac{\mathfrak{w}^2}{\rho^3 f}\mathfrak{F}^2 + \frac{8}{\rho}\frac{f}{\tilde{f}}\left(\frac{\tilde{f}^2}{f^2} - \frac{\mathfrak{q}^2}{\mathfrak{w}^2}\right) = 0\,, \tag{5.4}$$

where $\mathfrak{F}$ is defined in (3.15) with $F = \rho^3 f$. The boundary condition for regularity at the horizon becomes $\mathfrak{F}(1) = -\frac{4i}{\mathfrak{w}}$ and the spectral function is given by the asymptotic limit in (3.17).

Next we can repeat the analysis of section 3.1 to extract $\Omega(\mathfrak{q})$ and $\Gamma(\mathfrak{q})$ from the spectral function — in particular, our results were derived using the structure of $\partial^3_{\mathfrak{w}}\mathfrak{R}$. The behaviour of the lowest lying mode are plotted in figure 19. The most striking features revealed there are a) the asymptotic velocity is precisely one and b) the width decreases with increasing $\mathfrak{q}$. Hence there is a remarkable contrast between this behaviour for the supergravity vector and that described for the D7-brane vector in section 3.1.

We should note that at $\mathfrak{q} = 0$ our approach here yields $(\Omega(0), \Gamma(0)) = (1.51, .85)$ while the precise analytic results are known to be $(\Omega_n(0), \Gamma_n(0)) = (n, n)$ [9]. Hence we have

JHEP06(2008)052

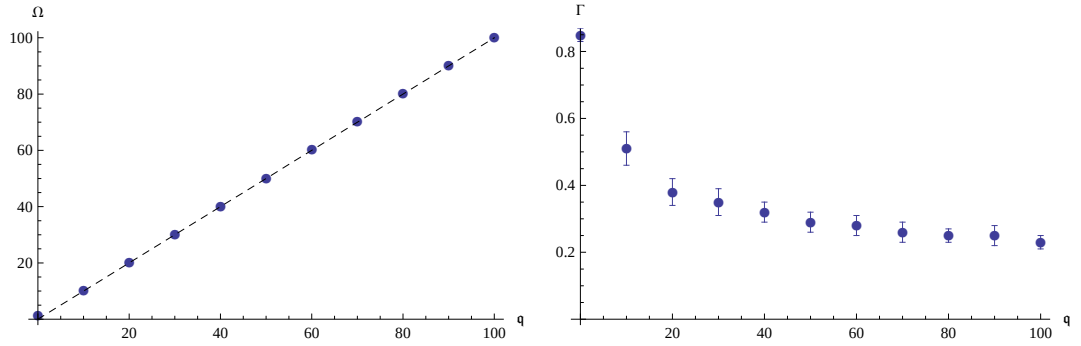

Figure 19: The energy $\Omega(\mathfrak{q})$ and width $\Gamma(\mathfrak{q})$ for the lowest lying mode for the supergravity gauge field. The black dashed line on the right corresponds to $\Omega = \mathfrak{q}$.

an indication of the potential errors in our spectral function results. We should note that an analytic expression for spectral function at $\mathfrak{q} = 0$ is also known [9] and our numerical calculation of spectral function agrees well with this result. However, it is not surprising that our technique for extracting the energy and width from $\mathfrak{A}$ is giving imprecise results here since we have $\Omega_n(0) = \Gamma_n(0)$ and further $\Delta\Omega \simeq \Gamma_n$ for the first few poles. We remain confident that the qualitative behaviour appearing in figure 19 is correct. In particular, precisely the same behaviour was first found for the supergravity modes studied in [27, 28], e.g., see figures 3 and 4 in [28].

We would like to understand these qualitative features from the structure of the effective potential in the Schrödinger equation (5.2). As shown in figure 18, one of the interesting features of V is that it develops a relatively flat plateau in the regime $0 < R_* < 1$, which corresponds to large values of ρ. Further, calculating the real part of the effective energy $\Omega_S = \mathrm{Re}(\mathfrak{w}^2) = \Omega^2 - \Gamma^2$ — see appendix A — for the lowest lying level, we find that this energy is just above the potential energy at the plateau. If we consider a WKB calculation of the corresponding wave-function, our intuition is confirmed about both of the qualitative features above. In particular, in this approximation, the amplitude of the wave-function would be given by [30]

$$|\psi|^2 \simeq \frac{1}{P(R_*)} = \frac{1}{\sqrt{\Omega_S - V(R_*)}} \tag{5.5}$$

where $P(R_*)$ is the classical momentum of the particle (with energy Ω_S) evaluated at the position R_*. Hence the amplitude of the wave-function is largest on the plateau and so it seems natural that the wave-function has its largest support in this region $0 < R_* < 1$. For large ρ, we have $R_* \sim 2\sqrt{2}/\rho$ and so the latter range corresponds to large ρ. Hence the radial profile of the corresponding excitation has its support primarily in the region where the geometry is very close to that of AdS_5 and the redshift effects are minimal. Hence it is not surprising that the asymptotic velocity of these excitations is one, i.e., the speed of light.

Quantitatively we may also observe from figure 18 that $V_{\text{plateau}} \sim \mathfrak{q}^2$ and so with a small width, we naturally have $\Omega_S \simeq \Omega^2 \simeq \mathfrak{q}^2$. Finally while V_{plateau} and Ω_S are rapidly rising with $\mathfrak{q}$, the value of the potential remains fixed at zero at the horizon which corresponds to $R_* \to \infty$. Hence eq. (5.5) indicates that the relative amplitude of the wave-function at the

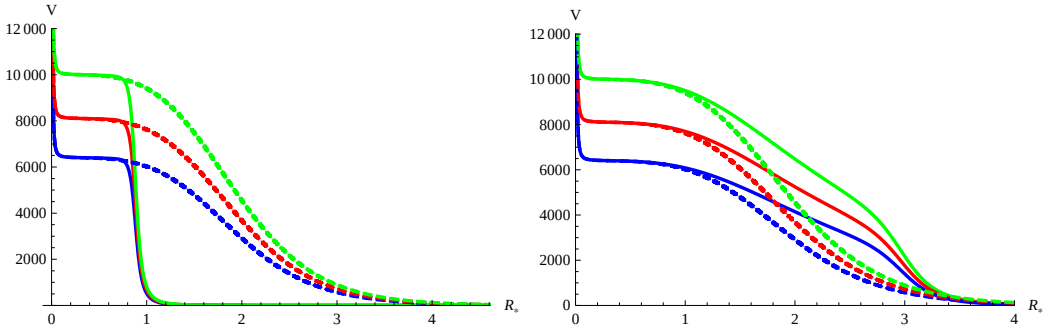

Figure 20: The solid lines correspond to the effective potential in case I (left) and V (right) for $\mathfrak{q} = 80$ (blue), 90 (red), 100 (green). The dashed lines correspond to the analogous supergravity potential in (5.3).

horizon is falling $|\psi|^2 \sim 1/\mathfrak{q}$. Hence it seems natural that the flux absorbed by the horizon should also be decreasing and hence the width of the state would be decreasing.

In principle, one could verify this intuitive picture with more detailed calculations to produce a better understanding of the precise normalization of the wave-function.[12] However, we now wish to apply our newly gained intuition to infer the behaviour of the meson dispersion relations at very large momentum. In figure 20, we compare the supergravity potential (5.3) to that for the analogous vector modes on the D7-brane for two of the cases (I and V) studied in section 3. In both cases, we are in a high-momentum regime where $\mathfrak{q} \gg \mathfrak{q}_{\rm crit}$ and so there is no evidence of the structure (i.e., a potential barrier and well in front of the horizon) discussed in section 4. While the structure of the potentials in figure 20 differs for $R_* > 1$ (i.e., deep in the bulk of the AdS_5 black hole), they are essentially identical for $R_* < 1$ (i.e., in the asymptotic region). In particular, the effective potential for the mesons also develops a plateau with $V_{\rm plateau} \sim \mathfrak{q}^2$ in this region. Hence it is natural to assume that at very high momentum, the poles characterising the thermal correlator for the meson operators will display a behaviour very similar to that found in the supergravity analysis. That is, $\Omega(\mathfrak{q})$ should exhibit an asymptotic velocity of one at very large $\mathfrak{q}$ and the widths $\Gamma(\mathfrak{q})$ should decrease as $\mathfrak{q}$ increases to very large values.

Hence we are led to conjecture that the full dispersion relations found by studying the quasinormal modes dual to the meson operators might take a form as illustrated in figure 21. In particular, the behaviour of the low-lying modes found for $\mathfrak{q} < \mathfrak{q}_{\rm crit}$ in section 3 should not be indicative of the overall structure. If we consider higher modes, i.e., modes which do not lie in the potential well of section 4, we expect that these modes will not exhibit a linear dispersion relation with slope $v_{\rm lim}$ in the $\mathfrak{q} < \mathfrak{q}_{\rm crit}$ regime as the low-lying modes do. Rather their dispersion relations will directly approach a linear behaviour in the $\mathfrak{q} \gg \mathfrak{q}_{\rm crit}$ regime with an asymptotic velocity of the speed of light. Similarly their widths are likely to be monotonically decreasing as found for the supergravity modes in [27, 28]. We have

[12] In the case of near-critical embeddings, a flat plateau in the potential produced similar effects in the quasinormal spectrum at $\mathfrak{q} = 0$ [29].

JHEP06(2008)052

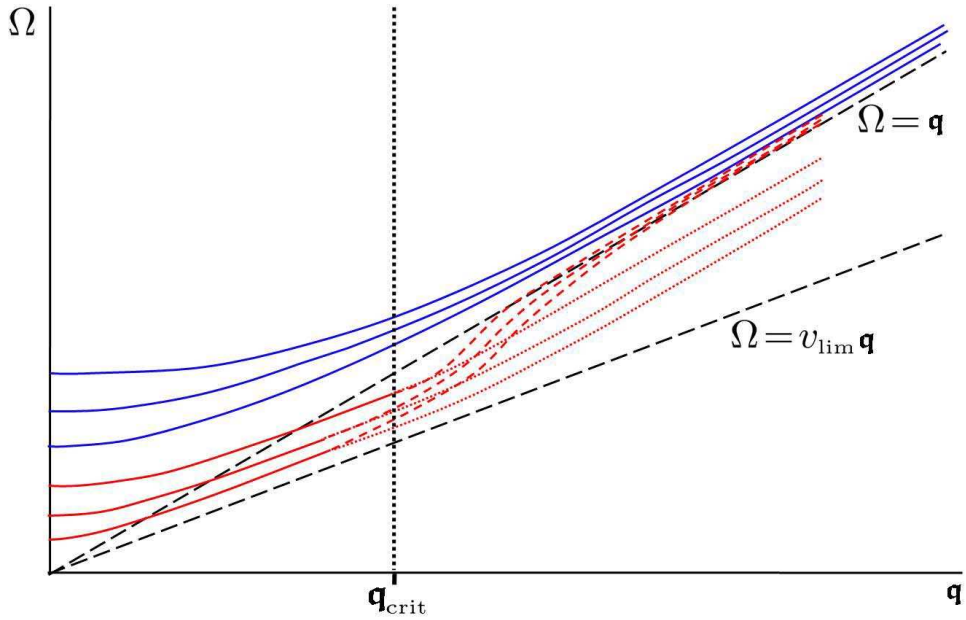

Figure 21: This plot shows possible behaviours of the dispersion relations beyond $\mathfrak{q}_{\rm crit}$. The lowest lying modes (red) exhibit $v_{\rm lim} < 1$ below $\mathfrak{q}_{\rm crit}$ but approach $\partial_{\mathfrak{q}}\Omega = 1$ in the regime $\mathfrak{q} > \mathfrak{q}_{\rm crit}$. The latter limiting behaviour may (dashed curves) or may not (dotted curves) exhibit 'superluminal' speeds, i.e., $\partial\Omega/\partial\mathfrak{q} > 1$. The higher modes (blue) directly approach the limit $\partial_{\mathfrak{q}}\Omega = 1$ in the regime $\mathfrak{q} > \mathfrak{q}_{\rm crit}$.

found some evidence of this qualitative behaviour for the higher modes from the spectral functions but we do not believe our results are quantitatively precise. There remains the interesting question of what should be the high-momentum behaviour of the poles corresponding to the low-lying modes, i.e., those which exhibit $v_{\rm lim} < 1$ for $\mathfrak{q} < \mathfrak{q}_{\rm crit}$. The behaviour suggested in figure 21 is that beyond $\mathfrak{q}_{\rm crit}$, $\Omega(\mathfrak{q})$ should also reach $v_{\rm asym} = 1$ for $\mathfrak{q} \gg \mathfrak{q}_{\rm crit}$. However, we can only speculate on precisely how this should arise. One possibility illustrated in figure 21 is that $\Omega(\mathfrak{q})$ should rise up and asymptote to $\Omega = \mathfrak{q}$, which would be similar to the behaviour exhibited by the sound mode in [21] — see their figure 5. This would require passing through a regime where $\partial_{\mathfrak{q}}\Omega > 1$, i.e., the group velocity appears to be superluminal, but of course, this need not correspond to a violation of causality — for example, see [31]. Another alternative also shown in figure 21 is that these modes approach $\partial_{\mathfrak{q}}\Omega|_{\rm lim} = 1$ asymptotically without passing through a regime with $\partial_{\mathfrak{q}}\Omega > 1$.

We add one further observation on the spectrum of the quasinormal eigenfrequencies. The poles corresponding to the quasiparticles discussed in section 4 corresponds to modes with support primarily behind the barrier in the effective potential (4.2). Further the discussion here also refers to modes with support primarily in the asymptotic region of the D7-brane. That is, the support of all of these modes is mainly above the narrow throat in D7-brane geometry. However, at least in the regime $\mathfrak{q} < \mathfrak{q}_{\rm crit}$, there should be additional poles corresponding to quasinormal modes whose support is predominantly in front of the potential barrier, i.e., in the narrow throat. These would be interpreted excitations of the effective string gas that is modeled by the throat [14]. These would be expected to

JHEP06(2008)052

have $\Gamma \sim \Omega$ and so would not lend themselves to a quasiparticle interpretation [4]. It would also be interesting to understand the behaviour of these quasinormal modes and their interplay with the modes with support above the throat as we move into the regime $\mathfrak{q} > \mathfrak{q}_{\rm crit}$. Certainly, as shown in figure 20, the structure of the effective potential differs from that in the supergravity problem for large R_* (small ρ), hence it could be that it still supports an additional set of modes in this regime with distinct physical characteristics.

6. Discussion

In this paper, we have used holographic techniques to calculate the spectral functions and to study the dispersion relations of meson quasiparticles moving through a thermal plasma of a strongly coupled $\mathcal{N} = 2$ super-Yang-Mills theory. The quasiparticle peaks in the spectral functions arise from poles in the corresponding thermal correlator (3.2) at $\Omega - i\Gamma$ in the lower half of the complex frequency plane. Considering the energy Ω and the width Γ as functions of the spatial momentum $\mathfrak{q}$, the broad picture which emerged was that there were two distinct regimes distinguished by a critical momentum $\mathfrak{q}_{\rm crit}$. In the low-momentum regime $\mathfrak{q} < \mathfrak{q}_{\rm crit}$, the spectral function exhibited clear quasiparticle peaks. By following their position and shape with growing $\mathfrak{q}$, we were able to estimate the the dispersion relations, $\Omega(\mathfrak{q})$ and $\Gamma(\mathfrak{q})$, for the low-lying resonances. In the high-momentum regime $\mathfrak{q} > \mathfrak{q}_{\rm crit}$, the poles have moved too far into the complex plane and no quasiparticle peaks are evident in the spectral functions. However, we examined the effective Schrödinger equation governing the dual quasinormal modes and provided some qualitative insight into the dispersion relations in this regime.

One of our key results for the $\mathfrak{q} < \mathfrak{q}_{\rm crit}$ regime is that the quasiparticles approach the same limiting velocity found for the case of stable mesons [7, 12]. This result emphasizes that this limiting velocity will be a universal feature in any holographic model. While the precise form of the limit may depend on the particular model, it arises from gravitational redshifting in the background geometry, as indicated by (1.1). Hence it will apply for any gauge theory excitations that have a dual description in terms of *radially localized* modes in the dual geometry. So, for example, this robust feature would also apply in the adjoint sector to 'glueball' excitations that are dual to a wavepacket of supergravity modes localized in the radial direction.

Of course, not all excitations of interest in a holographic model need not be radially localized. For example, massive quarks in the $\mathcal{N} = 2$ super-Yang-Mills theory (with $n_{\rm q} = 0$) are represented by extended strings stretching down from the D7-brane to the horizon in the dual gravitational description. Of course, the same gravitational redshift is observed to have interesting physical effects when these quarks are in motion — e.g., see [32]. Further, using holographic Wilson lines, a similar effect was observed to lead to the dissociation of a heavy quark bound state moving at a finite velocity through a strongly coupled $\mathcal{N} = 4$ plasma [33].

The second interesting observation for the low-lying mesons in the $\mathfrak{q} < \mathfrak{q}_{\rm crit}$ regime is that their widths show a dramatic increase as the momentum approaches $\mathfrak{q}_{\rm crit}$. In our holographic gravity model, the rise in Γ is easy to understand. As observed for the Minkowski

JHEP06(2008)052

embeddings [7], with finite $\mathfrak{q}$, the excitations on the probe D7-brane feel an extra potential which pushes the support of the radial profile of the mesons down to minimum radius on the brane. Intuitively, this can be understood as when the momentum is introduced, the brane fields carry extra local energy density and so feel a stronger gravitational force pulling them towards the horizon. As described in section 2.1, we have destabilized the mesons by introducing a narrow throat which extends down to the horizon from the point where the brane would have otherwise closed off. Hence the additional potential due to the momentum naturally pushes the meson fields down this throat making these states decay more quickly. This intuitive picture can be made more quantitative with the Schrödinger framework introduced in section 4. The latter approach also made clear that the potential barrier, which maintained the metastability of the quasiparticles, vanishes above some momentum. The disappearance of the barrier in the effective potential provides a precise mathematical criterion with which to define $\mathfrak{q}_{\rm crit}$. While this is a natural definition, we should add that the distinguishing momentum $\mathfrak{q}_{\rm crit}$ remains a rather qualitative concept and another definition was also considered in section 3.

In the high-momentum regime, our qualitative investigation of the effective Schrödinger equation suggests that the asymptotic velocity is $v_{\rm asym} = 1$ for $\mathfrak{q} \gg \mathfrak{q}_{\rm crit}$. Here the modes should be radially localized but evade having a limiting velocity less than the speed of light because they are not localized near the black hole horizon. Rather, our suggestion is that as $\mathfrak{q}$ increases to very large values, the support of quasinormal modes becomes increasingly focussed at very large radius, i.e., towards the AdS boundary, where the gravitational redshift becomes vanishingly small. This conjecture is largely based on making an analogy with similar supergravity fields for which some explicit results for the quasinormal frequencies are known [27, 28]. The latter results further suggest that in this high momentum regime the widths should decrease with increasing momentum. To clarify the details of the behaviour in this high-momentum regime, one would have to examine the quasinormal modes directly [25]. It would also be interesting to better understand the physical differences between the present case and that with $n_{\rm q} = 0$ in which the mesons are display $v_{\rm lim} < 1$ for arbitrarily large $\mathfrak{q}$.

Still given the present understanding, an interesting physical picture has emerged. Namely, in the low-momentum regime, the quasiparticles are strongly coupled to the deconfined plasma of the adjoint fields. The gravitational redshift leading to $v_{\rm lim} < 1$ is the geometric description of this strong coupling. An interesting problem would be to map the 'glue' cloud associated with these moving mesons, e.g., along the lines of [34]. We expect that the energy density of this halo must be rapidly increasing to maintain the meson's velocity at $v_{\rm lim} < 1$. However, in the high-momentum regime, the quasiparticles and the adjoint plasma are no longer strongly coupled to each other and the meson excitations can achieve the speed of light. Of course, the behaviour in this high-momentum regime restores the intuitive picture that one might acquire from considering the theory at weak coupling, namely, that at high momentum, the quasiparticles should be largely unaffected by the surrounding plasma.

In the low-momentum regime, the methods which we applied in section 3 allowed us to estimate not only the positions of the poles (from Ω and Γ) but also their residues

JHEP06(2008)052

A. The latter were found to decrease with increasing $\mathfrak{q}$, as illustrated in figure 13. As noted in [35], the parameter dependence of A can be important in determining the overall form of the spectral function and clearly here the fall in the residues plays a role in the disappearance of the resonances in the spectral functions. However, one might note these residues are indicative of the coupling of the relevant operator to the thermal bath, i.e., of how effective the operator is in generating the relevant quasiparticle excitations. Hence for the present purposes, we need not think of A as a physical characteristic of the quasiparticle itself.[13] In contrast, $\Omega(\mathfrak{q})$ and $\Gamma(\mathfrak{q})$ certainly characterize the basic physical behaviour of the quasiparticles. In particular, in order for a certain pole in the thermal correlator to be considered a quasiparticle in the first place, it must satisfy the Landau criterion $\Gamma \ll \Omega$. Intuitively, we may understand this requirement by observing that the corresponding wave function has a factor $\exp[-i\Omega t - \Gamma t]$. Hence with $\Gamma \ll \Omega$, there are a large number of oscillations before the excitation is damped out.

In section 3, we found another important reason that the quasiparticle peaks were quickly absorbed into the background is that the spacing between neighbouring poles shrinks with growing momentum, as is illustrated by the dispersion curves in figure 6. Certainly at a practical level identifying the peaks in the spectral functions requires $\Gamma \ll \Delta\Omega$ where $\Delta\Omega$ is the spacing between neighbouring poles (along the real axis). As illustrated with figure 10 for case VI, the peaks are begin to coalesce at roughly the point where they vanish from the spectral function. At this point, the poles of interest are not isolated and rather there are a large number of poles with roughly equal spacings and similarly growing widths, which produces some smooth continuum (rather than individual peaks). A quasiparticle interpretation is inappropriate then. Instead the infinite collection of poles is collectively generating the smooth background which remains in the spectral function.

It is interesting to consider how well the peaks of the spectral function were reconstructed given the estimates we produced for the relevant parameters in section 3. Figure 22 shows a typical peak which corresponds to case IV with $\mathfrak{q} = 50$. Also shown is the Breit-Wigner peak (3.3) reconstructed with various estimates of Ω, Γ and A, produced by examining $\partial^3_{\mathfrak{w}}\mathfrak{R}$ as described in section 3. While this reconstruction matches the shape of the peak near the maximum quite well, there are two other notable features which are quite apparent. First the reconstructed peak appears displaced slightly towards smaller $\mathfrak{w}$ relative to where $\partial_{\mathfrak{w}}\mathfrak{R} = 0$. Of course, this is to be expected since there is a rising background that also contributes to the spectral function. The second feature, which we found surprising, is that this background seems to be quite small. That is, the maximum of reconstructed peak matches very well with the maximum value of the spectral function. More generally, we found that using our parameter estimates to reconstruct the quasiparticle peaks gave a background that was typically only between 10 and 20% under the top of the peak.

Given the limitations in studying the spectral functions, it would also be very interesting to investigate the quasinormal modes directly, following e.g., [10, 26]. While this

[13] However, this coupling may become physically relevant for a certain quasiparticle decay channel if in the underlying theory the operator couples to other physical fields, e.g., photons [36].

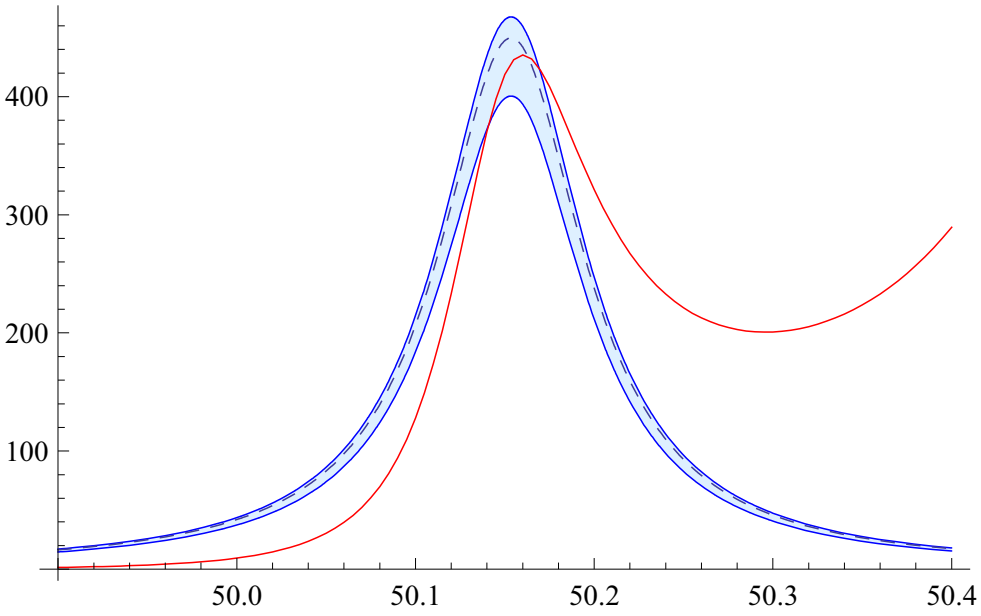

Figure 22: The red curve shows the spectral function for case IV with $\mathfrak{q} = 50$. The blue region shows the peak (3.20) as reconstructed with the parameters Ω, Γ and A. calculated in section 3. The center (dashed) line in the shaded region uses $(\Omega, \Gamma, A) = (\mathfrak{w}_0, \bar{\Gamma}, A_1)$. The bottom (solid) boundary of the shaded region is generated with $(\Omega, \Gamma, A) = (\mathfrak{w}_0, \bar{\Gamma} + \Delta\Gamma, A_{2,+})$, while the top (thick solid) boundary uses $(\Omega, \Gamma, A) = (\mathfrak{w}_0, \bar{\Gamma} - \Delta\Gamma, A_{2,-})$.

$\mathfrak{q}$	$\mathfrak{w}_{\rm qn}$	$\mathfrak{w}$
0	$1.031 - 0.042i$	$1.034 - 0.042i$
0.5	$1.085 - 0.05i$	$1.091 - 0.049i$
1	$1.227 - 0.072i$	$1.234 - (0.072 \pm 0.001)i$
1.5	$1.408 - 0.112i$	$1.426 - (0.115 \pm 0.001)i$
2	$1.596 - 0.164i$	$1.644 - (0.186 \pm 0.004)i$
2.2	$1.671 - 0.187i$	$1.730 - (0.220 \pm 0.010)i$

Table 3: Quasinormal modes obtained as poles in the spectral function for case VI.

presents additional technical challenges, it would allow for a detailed verification of the quasiparticle dispersion relations found here in the low-momentum regime but also to establish the behaviour conjectured for the high-momentum regime [25]. At this stage, we would like to make the following observation. It is possible to extract the quasinormal modes directly from the spectral function. If $\mathfrak{w} = \Omega - i\Gamma$ is a quasinormal mode, this will show up as a pole in the spectral function $\mathfrak{A}$. Since we have an approximate idea about the location of the peaks from the spectral functions as well as an idea about the widths, we have a reasonable initial guess which can be fine-tuned to locate the pole. It turns out that for larger $\mathfrak{q}$'s, the fine-tuning required increases. Table 3 is a comparison between this method and the method of estimating parameters from $\partial^3_{\mathfrak{w}}\mathfrak{A}$ for case VI.

As is clear from the table, for larger $\mathfrak{q}$ the quasinormal mode analysis predicts a lower Γ.

JHEP06(2008)052

While we see a dramatic rise in the width Γ of quasiparticles in the present model, it remains to understand if this increase is a universal feature which emerges in any holographic model. Of course, an even more important question, is whether or not such an effect is realized in the strongly coupled quark-gluon plasma of QCD. Certainly both of these questions deserve further investigation.

At present, investigating spectral functions with non-zero momentum is an important direction of ongoing research [37, 38]. Only partial results are available since the existing methods seem to be inadequate for this problem. Recent results, which generally use the so-called potential approach, indicate the spectral functions flatten with increasing momentum [37, 38] — an effect consistent with our present findings.

Of course, if these effects found here in our holographic studies are realized in QCD, they would have interesting implications for experiments at RHIC and LHC. In particular, as suggested in [12, 33], they could lead to a significant additional suppression of J/Ψ or other heavy quark mesons with large transverse momenta. Certainly a critical momentum where the quasiparticle widths rise dramatically would produce a dramatic effect. Another potentially interesting effect was outlined in [36]. One distinct feature resulting from a limiting velocity $v_{\rm lim} < 1$ is that the four momenta of quasiparticles become null at some point. For example, if we drop the higher order terms in the asymptotic dispersion relation (3.19), then the quasiparticle's dispersion relation crosses the null cone at

$$\Omega = \frac{a_i}{1 - v_{\rm lim}} = \mathfrak{q}\,. \tag{6.1}$$

Following the holographic techniques of [39], one then finds that this crossing of the null cone produces a peak in photon production from charged quasiparticles [36]. Such a resonance would then be a distinctive experimental signature of $v_{\rm lim} < 1$. Of course, as speculated in figure 21, the dispersion relations may cross the null cone twice and exhibit a regime $\partial_{\mathfrak{q}}\Omega > 1$, which may produce further dramatic signals.

From (6.1), we observe that this enhancement is pushed to infinite momentum as $v_{\rm lim}$ approaches one. Hence, if $v_{\rm lim}$ is still close to one at RHIC or LHC, this signal would only appear at very large momenta. Further, if the quasiparticle width increases too quickly, this enhancement in the photon production would likely be washed out. The point where the quasiparticle 'four-momentum' is null is indicated in figure 9 for the four cases in table (2). For cases IV, V and VI, one indeed finds that this null momentum seems to lie in the regime where the width is growing rapidly, while case VII seems to present an exception to this rule. Further as can be seen in figure 7 for the more stable cases presented in table (1), the quasiparticle dispersion relations seem to cross the null cone well away from the maximum momentum. Hence it seems this question also requires further study.

Acknowledgments

It is a pleasure to thank Andreas Karch, Hong Liu, Juan Maldacena, Amanda Peet, Peter Petreczky, Krishna Rajagopal, Lennie Susskind and especially Andrei Starinets for useful correspondence and conversations. Research at Perimeter Institute is supported by the

JHEP06(2008)052

Government of Canada through Industry Canada and by the Province of Ontario through the Ministry of Research & Innovation. RCM also acknowledges support from an NSERC Discovery grant and funding from the Canadian Institute for Advanced Research. RCM thanks the organizers of *Miami 2007* and the *LindeFest* for the opportunity to speak on this work. AS also thanks the organizers of *Quark Matter 2008* for the opportunity to speak on this work.

A. WKB approximation

In this section, we outline how WKB calculations might be applied to produce an approximate value for the quasinormal eigenfrequencies. Recall that these eigenfrequencies are determined by solving the relevant wave equation with boundary conditions of an ingoing wave at the horizon and of only the normalizable mode asymptotically [10]. In (4.1), the relevant wave equation for the transverse vector modes has been caste into the form of a one-dimensional Schrödinger with an effective energy

$$\begin{aligned} E_{\text{eff}} &= \Omega_S - i\Gamma_S \\ &= \mathfrak{w}^2 = \Omega^2 - \Gamma^2 - 2i\,\Omega\Gamma\,. \end{aligned} \tag{A.1}$$

The quasinormal eigenfrequencies correspond to the positions of the poles in the thermal correlators and so we denote the eigenfrequency $\mathfrak{w} = \Omega - i\Gamma$ above in keeping with the notation of section 3.

In a typical case of interest, the effective potential has a form as illustrated in figures 14 or 17, with a well that is separated from the horizon at $\rho = 1$ by a large potential barrier. The relevant modes corresponding to metastable meson states are then bound states with support primarily in the potential well but which slowly tunnel out through the barrier. The idea then is to approximately determine E_{eff} for these modes using WKB techniques — see, e.g., [30].

First the real part of the effective energy Ω_S is obtained by fine-tuning Ω_S so that

$$\int_{R_2}^{R_3} dR_* \sqrt{\Omega_S - V(R_*)} = \left(n - \frac{1}{2}\right)\,\pi\,, \tag{A.2}$$

where R_2, R_3 are the classical turning points in the potential well where $V = \Omega_S$. The first peak in one of the spectral functions would correspond to $n = 1$. Next within the WKB approximation, the decay rate Γ_S is defined as [30]

$$\Gamma_S = \mathcal{N} \exp(-2 \int_{R_1}^{R_2} dR_* \sqrt{V - \Omega_S})\,. \tag{A.3}$$

Here R_1, R_2 denote classical turning points in the barrier and implicitly Ω_S denotes the WKB energy eigenvalue determined by (A.2). The normalization constant $\mathcal{N}$ is given by

$$\mathcal{N}^{-1} = \int_{R_2}^{R_3} \frac{dR_*}{\sqrt{V - \Omega_S}}\,. \tag{A.4}$$

JHEP06(2008)052

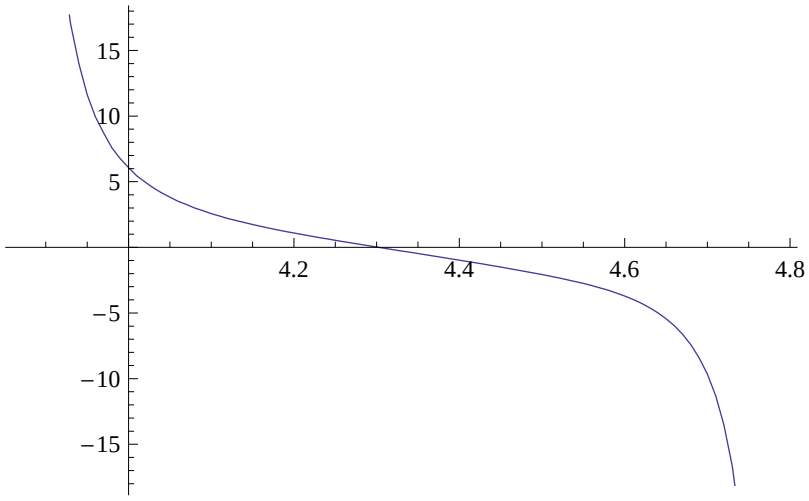

Figure 23: The validity of the WKB approximation can be tested by considering k'/k^2 versus ρ. These are plotted here inside the barrier for $\tilde{d} = 0.25, \chi_0 = 0.99$. At the turning points a deviation from unity is expected but significant deviations are seen well away from those points, making the WKB approximation (A.3) unreliable.

Given these WKB results for the Schrödinger problem, we may use (A.1) to determine the eigenfrequency for the corresponding quasinormal mode:

$$\Omega^2 = \frac{\Omega_S}{2}\left[1+\sqrt{1+\Gamma_S^2/\Omega_S^2}\right] \simeq \Omega_S\left[1+\frac{1}{4}\frac{\Gamma_S^2}{\Omega_S^2}\right], \tag{A.5}$$
$$\Gamma = \Gamma_S/2\Omega \simeq \frac{\Gamma_S}{2\sqrt{\Omega_S}}\left[1-\frac{1}{8}\frac{\Gamma_S^2}{\Omega_S^2}\right].$$

In the second of each of these expressions, we have presented the leading terms in an expansion with $\Gamma_S/\Omega_S \ll 1$, which is a necessary condition for the validity of the WKB approximation. The latter calculation focussed on the well and barrier appearing in the effective potential $V(R_*)$ while completely ignoring the horizon. In the results of, e.g., [9, 10, 21], one sees that for an effective potential is a monotonically rising function $\Gamma \sim \Omega$ or $\Gamma_S > \Omega_S$. Clearly, the horizon has an important effect in determining the eigenfrequencies and, in particular, the decay width in this situation. Hence one cannot expect that the WKB calculations outlined above will be reliable in this regime. In particular, when the barrier is getting small, the WKB calculation would yield an tunnelling rate that becomes large but the precise value of Γ_S would depend crucially on the structure of the potential near and the boundary conditions at the horizon.

However, as discussed in section 4, there are additional subtleties in the WKB approximation. For the WKB calculation of the tunnelling rate to be valid, the change of the momentum over a wavelength must be small compared to the momentum itself. That is, if we define $k = \sqrt{V - \mathfrak{w}^2}$ under the barrier, then we must require [30],

$$\frac{|k'(R_*)|}{k(R_*)^2} \ll 1\,. \tag{A.6}$$

JHEP06(2008)052

Unfortunately, in the examples considered in the paper, this condition is typically not satisfied for a large region within the barrier, essentially because the shoulders of the barrier are too steep — e.g., see figure 23. This makes the WKB calculation (A.3) of Γ_S unreliable, in particular in the regime where Γ begins to increase dramatically. We have done WKB calculations of Γ in various cases when $\Gamma/\Gamma_0 \sim 1$ and found the WKB results agreed with those in section 3 to within roughly 15% despite the issues discussed above. Note that the condition (A.6) is quite generally satisfied for the calculation (A.2) of Ω_S, the real part of the effective energy. Hence in the regime $\Gamma_S/\Omega_S \ll 1$, the WKB approach would still provide an accurate approximation for $\Omega \simeq \Omega_S^{1/2}$. Further, one can still gain some qualitative insight into Γ by considering when the barrier disappears in the effective potential, as discussed in section 4.

References

[1] J.M. Maldacena, *The large-N limit of superconformal field theories and supergravity*, *Adv. Theor. Math. Phys.* **2** (1998) 231 [*Int. J. Theor. Phys.* **38** (1999) 1113] [hep-th/9711200].

[2] O. Aharony, S.S. Gubser, J.M. Maldacena, H. Ooguri and Y. Oz, *Large-N field theories, string theory and gravity*, *Phys. Rept.* **323** (2000) 183 [hep-th/9905111].

[3] P. Kovtun, D.T. Son and A.O. Starinets, *Viscosity in strongly interacting quantum field theories from black hole physics*, *Phys. Rev. Lett.* **94** (2005) 111601 [hep-th/0405231];
Holography and hydrodynamics: diffusion on stretched horizons, *JHEP* **10** (2003) 064 [hep-th/0309213].

[4] C.P. Herzog, A. Karch, P. Kovtun, C. Kozcaz and L.G. Yaffe, *Energy loss of a heavy quark moving through $N = 4$ supersymmetric Yang-Mills plasma*, *JHEP* **07** (2006) 013 [hep-th/0605158];
H. Liu, K. Rajagopal and U.A. Wiedemann, *Calculating the jet quenching parameter from AdS/CFT*, *Phys. Rev. Lett.* **97** (2006) 182301 [hep-ph/0605178];
S.S. Gubser, *Drag force in AdS/CFT*, *Phys. Rev.* **D 74** (2006) 126005 [hep-th/0605182];
J. Casalderrey-Solana and D. Teaney, *Heavy quark diffusion in strongly coupled $N = 4$ Yang-Mills*, *Phys. Rev.* **D 74** (2006) 085012 [hep-ph/0605199].

[5] J. Babington, J. Erdmenger, N.J. Evans, Z. Guralnik and I. Kirsch, *Chiral symmetry breaking and pions in non-supersymmetric gauge/gravity duals*, *Phys. Rev.* **D 69** (2004) 066007 [hep-th/0306018];
M. Kruczenski, D. Mateos, R.C. Myers and D.J. Winters, *Towards a holographic dual of large-N_c QCD*, *JHEP* **05** (2004) 041 [hep-th/0311270];
I. Kirsch, *Generalizations of the AdS/CFT correspondence*, *Fortschr. Phys.* **52** (2004) 727 [hep-th/0406274].

[6] D. Mateos, R.C. Myers and R.M. Thomson, *Holographic phase transitions with fundamental matter*, *Phys. Rev. Lett.* **97** (2006) 091601 [hep-th/0605046].

[7] D. Mateos, R.C. Myers and R.M. Thomson, *Thermodynamics of the brane*, *JHEP* **05** (2007) 067 [hep-th/0701132].

[8] D. Mateos, R.C. Myers and R.M. Thomson, *Holographic viscosity of fundamental matter*, *Phys. Rev. Lett.* **98** (2007) 101601 [hep-th/0610184];

JHEP06(2008)052

T. Albash, V.G. Filev, C.V. Johnson and A. Kundu, *A topology-changing phase transition and the dynamics of flavour*, *Phys. Rev.* **D 77** (2008) 066004 [hep-th/0605088];
A. Karch and A. O'Bannon, *Chiral transition of $N = 4$ super Yang-Mills with flavor on a 3-sphere*, *Phys. Rev.* **D 74** (2006) 085033 [hep-th/0605120];
T. Albash, V.G. Filev, C.V. Johnson and A. Kundu, *Global currents, phase transitions and chiral symmetry breaking in large-N_c gauge theory*, hep-th/0605175;
A. Karch and A. O'Bannon, *Metallic AdS/CFT*, *JHEP* **09** (2007) 024 [arXiv:0705.3870];
A. O'Bannon, *Hall conductivity of flavor fields from AdS/CFT*, *Phys. Rev.* **D 76** (2007) 086007 [arXiv:0708.1994];
J. Erdmenger, N. Evans, I. Kirsch and E. Threlfall, *Mesons in gauge/gravity duals — A review*, *Eur. Phys. J.* **A35** (2008) 81 [arXiv:0711.4467].

[9] R.C. Myers, A.O. Starinets and R.M. Thomson, *Holographic spectral functions and diffusion constants for fundamental matter*, *JHEP* **11** (2007) 091 [arXiv:706.0162].

[10] C. Hoyos-Badajoz, K. Landsteiner and S. Montero, *Holographic meson melting*, *JHEP* **04** (2007) 031 [hep-th/0612169].

[11] T. Umeda, K. Nomura and H. Matsufuru, *Charmonium at finite temperature in quenched lattice QCD*, *Eur. Phys. J.* **C 39S1** (2005) 9 [hep-lat/0211003];
M. Asakawa and T. Hatsuda, *J_ψ and η_c in the deconfined plasma from lattice QCD*, *Phys. Rev. Lett.* **92** (2004) 012001 [hep-lat/0308034];
S. Datta, F. Karsch, P. Petreczky and I. Wetzorke, *Behavior of charmonium systems after deconfinement*, *Phys. Rev.* **D 69** (2004) 094507 [hep-lat/0312037];
A. Jakovac, P. Petreczky, K. Petrov and A. Velytsky, *On charmonia survival above deconfinement*, hep-lat/0603005;
G. Aarts et al., *Charmonium spectral functions in $N_f = 2$ QCD at high temperature*, PoS(LAT2006)126 [hep-lat/0610065];
G. Aarts, C. Allton, J. Foley, S. Hands and S. Kim, *Spectral functions at non-zero momentum in hot QCD*, PoS(LAT2006)134 [hep-lat/0610061];
P. Petreczky, *Lattice QCD at finite temperature*, *Nucl. Phys.* **A 785** (2007) 10 [hep-lat/0609040];
G. Aarts, C. Allton, J. Foley, S. Hands and S. Kim, *Spectral functions at small energies and the electrical conductivity in hot, quenched lattice QCD*, *Phys. Rev. Lett.* **99** (2007) 022002 [hep-lat/0703008];
H.B. Meyer, *A calculation of the shear viscosity in SU(3) gluodynamics*, *Phys. Rev.* **D 76** (2007) 101701 [arXiv:0704.1801];
G. Aarts, C. Allton, M.B. Oktay, M. Peardon and J.-I. Skullerud, *Charmonium at high temperature in two-flavor QCD*, *Phys. Rev.* **D 76** (2007) 094513 [arXiv:0705.2198];
H. Satz, *Colour deconfinement and quarkonium binding*, *J. Phys.* **G 32** (2006) R25 [hep-ph/0512217].

[12] Q.J. Ejaz, T. Faulkner, H. Liu, K. Rajagopal and U.A. Wiedemann, *A limiting velocity for quarkonium propagation in a strongly coupled plasma via AdS/CFT*, *JHEP* **04** (2008) 089 [arXiv:0712.0590].

[13] S. Kobayashi, D. Mateos, S. Matsuura, R.C. Myers and R.M. Thomson, *Holographic phase transitions at finite baryon density*, *JHEP* **02** (2007) 016 [hep-th/0611099].

[14] D. Mateos, S. Matsuura, R.C. Myers and R.M. Thomson, *Holographic phase transitions at finite chemical potential*, *JHEP* **11** (2007) 085 [arXiv:0709.1225].

JHEP06(2008)052

[15] J. Erdmenger, M. Kaminski and F. Rust, *Holographic vector mesons from spectral functions at finite baryon or isospin density*, *Phys. Rev.* **D 77** (2008) 046005 [arXiv:0710.0334].

[16] Y. Hatta, E. Iancu and A.H. Mueller, *Deep inelastic scattering off a $N = 4$ SYM plasma at strong coupling*, *JHEP* **01** (2008) 063 [arXiv:0710.5297]; *Jet evolution in the $N = 4$ SYM plasma at strong coupling*, *JHEP* **05** (2008) 037 [arXiv:0803.2481].

[17] O. Aharony, A. Fayyazuddin and J.M. Maldacena, *The large-N limit of $N = 2, 1$ field theories from three-branes in F-theory*, *JHEP* **07** (1998) 013 [hep-th/9806159];
A. Karch and L. Randall, *Open and closed string interpretation of SUSY CFT's on branes with boundaries*, *JHEP* **06** (2001) 063 [hep-th/0105132];
A. Karch and E. Katz, *Adding flavor to AdS/CFT*, *JHEP* **06** (2002) 043 [hep-th/0205236].

[18] M. Kruczenski, D. Mateos, R.C. Myers and D.J. Winters, *Meson spectroscopy in AdS/CFT with flavour*, *JHEP* **07** (2003) 049 [hep-th/0304032].

[19] A. Karch and A. O'Bannon, *Holographic thermodynamics at finite baryon density: some exact results*, *JHEP* **11** (2007) 074 [arXiv:0709.0570].

[20] D.T. Son and A.O. Starinets, *Viscosity, black holes and quantum field theory*, *Ann. Rev. Nucl. Part. Sci.* **57** (2007) 95 [arXiv:0704.0240].

[21] P.K. Kovtun and A.O. Starinets, *Quasinormal modes and holography*, *Phys. Rev.* **D 72** (2005) 086009 [hep-th/0506184].

[22] D.T. Son and A.O. Starinets, *Minkowski-space correlators in AdS/CFT correspondence: recipe and applications*, *JHEP* **09** (2002) 042 [hep-th/0205051].

[23] D. Teaney, *Finite temperature spectral densities of momentum and R-charge correlators in $N = 4$ Yang-Mills theory*, *Phys. Rev.* **D 74** (2006) 045025 [hep-ph/0602044];
P. Kovtun and A. Starinets, *Thermal spectral functions of strongly coupled $N = 4$ supersymmetric Yang-Mills theory*, *Phys. Rev. Lett.* **96** (2006) 131601 [hep-th/0602059].

[24] D. Birmingham, I. Sachs and S.N. Solodukhin, *Conformal field theory interpretation of black hole quasi-normal modes*, *Phys. Rev. Lett.* **88** (2002) 151301 [hep-th/0112055].

[25] R.C. Myers and A. Sinha, in preparation.

[26] N. Evans and E. Threlfall, *Mesonic quasinormal modes of the Sakai-Sugimoto model at high temperature*, arXiv:0802.0775.

[27] A. Núñez and A.O. Starinets, *AdS/CFT correspondence, quasinormal modes and thermal correlators in $N = 4$ SYM*, *Phys. Rev.* **D 67** (2003) 124013 [hep-th/0302026].

[28] A.O. Starinets, *Quasinormal modes of near extremal black branes*, *Phys. Rev.* **D 66** (2002) 124013 [hep-th/0207133].

[29] A. Paredes, K. Peeters and M. Zamaklar, *Mesons versus quasi-normal modes: undercooling and overheating*, *JHEP* **05** (2008) 027 [arXiv:0803.0759].

[30] See, for example, E. Merzbacher, *Quantum mechanics*, John Wiley & Sons, U.S.A. (1967).

[31] R. Fox, C.G. Kuper and S.G. Lipson, *Faster-than-light group velocities and causality violation*, *Proc. Roy. Soc. Lond.* **A 316** (1970) 515; *Do faster-than-light group velocities imply violation of causality?*, *Nature* **223** (1969) 597.

JHEP06(2008)052

[32] S.S. Gubser, *Momentum fluctuations of heavy quarks in the gauge-string duality*, *Nucl. Phys.* **B 790** (2008) 175 [hep-th/0612143];
H. Liu, K. Rajagopal and U.A. Wiedemann, *Wilson loops in heavy ion collisions and their calculation in AdS/CFT*, *JHEP* **03** (2007) 066 [hep-ph/0612168];
P.C. Argyres, M. Edalati and J.F. Vazquez-Poritz, *Spacelike strings and jet quenching from a Wilson loop*, *JHEP* **04** (2007) 049 [hep-th/0612157];
J. Casalderrey-Solana and D. Teaney, *Transverse momentum broadening of a fast quark in a $N = 4$ Yang-Mills plasma*, *JHEP* **04** (2007) 039 [hep-th/0701123].

[33] H. Liu, K. Rajagopal and U.A. Wiedemann, *An AdS/CFT calculation of screening in a hot wind*, *Phys. Rev. Lett.* **98** (2007) 182301 [hep-ph/0607062];
K. Peeters, J. Sonnenschein and M. Zamaklar, *Holographic melting and related properties of mesons in a quark gluon plasma*, *Phys. Rev.* **D 74** (2006) 106008 [hep-th/0606195];
M. Chernicoff, J.A. Garcia and A. Guijosa, *The energy of a moving quark-antiquark pair in an $N = 4$ SYM plasma*, *JHEP* **09** (2006) 068 [hep-th/0607089].

[34] S.S. Gubser and A. Yarom, *Linearized hydrodynamics from probe-sources in the gauge-string duality*, arXiv:0803.0081.

[35] I. Amado, C. Hoyos-Badajoz, K. Landsteiner and S. Montero, *Residues of correlators in the strongly coupled $N = 4$ plasma*, *Phys. Rev.* **D 77** (2008) 065004 [arXiv:0710.4458].

[36] D. Mateos and L. Patino, *Bright branes for strongly coupled plasmas*, *JHEP* **11** (2007) 025 [arXiv:0709.2168].

[37] S. Datta, F. Karsch, S. Wissel, P. Petreczky and I. Wetzorke, *Charmonia at finite momenta in a deconfined plasma*, hep-lat/0409147;
G. Aarts, C. Allton, J. Foley, S. Hands and S. Kim, *Spectral functions at non-zero momentum in hot QCD*, PoS(LAT2006)134 [hep-lat/0610061]; *Meson spectral functions at nonzero momentum in hot QCD*, *Nucl. Phys.* **A 785** (2007) 202 [hep-lat/0607012];
G. Aarts, S. Hands, S.-Y. Kim and J.M. Martinez Resco, *On meson spectral functions at high temperature and nonzero momentum*, PoS(LAT2005)182 [hep-lat/0509062];
W.M. Alberico, A. Beraudo, P. Czerski and A. Molinari, *Finite momentum meson correlation functions in a QCD plasma*, *Nucl. Phys.* **A 775** (2006) 188 [hep-ph/0605060];
W.M. Alberico, A. Beraudo, A. Czerska, P. Czerski and A. Molinari, *Meson screening masses in the interacting QCD plasma*, *Nucl. Phys.* **A 792** (2007) 152 [hep-ph/0703298].

[38] P. Petreczky, private communication.

[39] S. Caron-Huot, P. Kovtun, G.D. Moore, A. Starinets and L.G. Yaffe, *Photon and dilepton production in supersymmetric Yang-Mills plasma*, *JHEP* **12** (2006) 015 [hep-th/0607237].

JHEP06(2008)052